



Environmental Physics IUP

Master Thesis

**Analysis of NO_x emission sources of Bremen using
WRF-Chem and DOAS**

Simon Bittner

University Bremen

Department 01: Physics/Electrical Engineering

simon-bittner@gmx.de

6023369

First Consultant:
Prof. M. Vrekoussis

Second Consultant:
PD Dr. A. Richter

November 7, 2022

Contents

1	Introduction	1
2	Theory	3
2.1	Chemical foundations	3
2.2	Experimental foundations	7
2.3	Modeling foundations	11
3	Methodology	17
3.1	Previous work	17
3.2	Bicycle DOAS measurements	18
3.3	DOAS data retrieval	24
3.4	Calculation of emissions	27
3.5	WRF-Chem settings and input data	30
3.6	Evaluation of WRF-Chem output	33
3.7	Plume modeling with FLEXPART-WRF	34
4	Results	37
4.1	DOAS measurements results	37
4.2	Comparison of calculated emissions	43
4.3	Comparison of WRF-Chem output with observations	44
4.4	Assessing importance of the waste incineration plant as an emitter	49
5	Discussion	53
5.1	Emission calculation	53
5.2	WRF-Chem output	55
5.3	Assessment on importance	56
6	Conclusion & Outlook	59
7	Acknowledgements	61
	Appendix	75

List of Abbreviations

AMF Air Mass Factor

B3dCTM Bremen 3d Chemistry Transport Model

CCD Charge-Coupled Device

DOAS Differential Optical Absorption Spectroscopy

DWD Deutscher Wetterdienst

ERA5T ECMWF Reanalysis v5 Data

FLEXPART Flexible Particle Dispersion Model

MAX-DOAS Multi-Axis DOAS

NCAR National Center for Atmospheric Research

NWP Numerical Weather Prediction

PRTR Pollutant Release and Transfer Register

SZA Solar Zenith Angle

TROPOMI Tropospheric Monitoring Instrument

VOC Volatile Organic Compound

WACCM Whole Atmosphere Community Climate Model

WPS WRF Preprocessing System

WRF Weather Research and Forecasting Model

Chapter 1

Introduction

As urbanization increases, health issues that can arise in a polluted environment make the study of air quality a top priority [13, 14, 33, 110]. The link between air quality and health began being investigated around the middle of the 20th century. The great smog (smoke and fog) disasters of Belgium in 1930, Donora in 1948 (USA) and London in 1952 (UK), made it clear that high concentrations of pollutants combined with stable stratification and low wind speeds can be fatal even over short periods [13, 101]. Of the disasters mentioned, the London case stands out: Concentrations of several thousand $\mu\text{g m}^{-3}$ sulfur dioxide and smoke led to around 12 000 deaths over the following years [14]. Given the severe impacts of air pollution, countries, like the USA, are restricting anthropogenic emissions of pollutants to improve the overall air quality and mitigate resulting health issues [102].

The introduction of air quality standards resulted in a significant decrease in overall emissions in the USA. Since then summer smog, a mixture of ozone, secondary organic aerosols, and their gaseous precursors in the presence of light [110], attracted attention [14]. The list of sources for pollutants is long, e.g., vehicles, fossil fuel combustion, and industrial solvent use. Additionally, natural sources contribute to the formation of ozone by emitting certain volatile organic compounds. [110]

As climate change influences ozone formation, it is expected that photochemical smog events will likely worsen in the future. Zhang, Wei, and Fang [110] found that a warming climate favors stagnant atmospheric conditions, hence the accumulation of ozone. Furthermore, the reactions involved in ozone production are sensitive to temperature as well as solar intensity, which leads to higher ozone production [110]. The WHO lists five major air pollutants: particulate matter pollution (PM), ground-level ozone (O_3), carbon monoxide (CO), sulfur oxides (SO_x) and nitrogen oxides (NO_x) [109].

This work focuses on nitrogen oxides for two specific emission sources in Bremen (Germany), out of which one source is analyzed in detail with the help of a state-of-the-art meteorological model coupled with a chemical mechanism. Based on measurements with Differential Optical Absorption Spectroscopy, the annual emissions of the airport and the waste incineration plant are calculated. The analysis is complemented by an assessment of the waste incineration plant concerning its local impact on the air quality. Both approaches are combined to receive two different perspectives on the current understanding of the impact of NO_x emissions on air quality in Bremen.

This thesis is structured as follows. First, the theoretical foundations of the relevant NO_x chemistry, the applied experimental method, and the used modeling tools are established. Afterward, the details of the approach of this work are described. This chapter is followed by the presentation of the results and their discussion. Finally, the study finishes with a summary of the main findings and future directions.

Chapter 2

Theory

This chapter elaborates on the theoretical foundations for the master thesis. The first section discusses tropospheric ozone and its precursors, NO_x and VOC, in detail and illustrates how they interact. The second section lays the groundwork for the experimental setup later. Here, the different processes influencing atmospheric absorption and scattering, as well as the theory of the DOAS method, are described. It is followed by an introduction to atmospheric models, their properties and their applications.

2.1 Chemical foundations

Ground-level ozone (O_3) impacts air quality and health [13, 14, 110]. Zhang, Wei, and Fang [110] state that long-term exposure at regulatory limits (US: 70 ppb¹ [103]) is associated with the development of asthma and premature deaths due to respiratory illnesses and cardiovascular diseases. Apart from that, ground-level ozone negatively impacts vegetation and reduces the crop yield in agriculture [31]. The tropospheric chemistry of ozone is complex, with many influencing factors including the precursor species NO_x , VOCs, and CO.

2.1.1 Nitrogen oxides

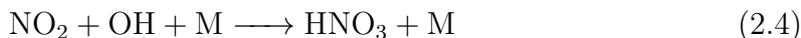
One important group of precursors is nitrogen oxide radicals. The chemical family ($\text{NO}_x \equiv \text{NO} + \text{NO}_2$) is used to group the nitrogen oxides into one convenient quantity as the two species rapidly convert into each other. The interconversion is called a null cycle because it does not influence the atmospheric composition [9]. It can be

¹8-h daily max

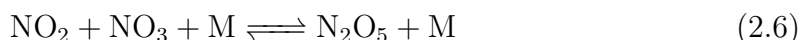
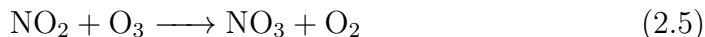
described via the following reactions:



The major NO_x sources in the troposphere are combustion, lightning and microbiological processes in soils, of which combustion is the dominant one [9]. The lifetime of NO_x ranges from approximately a day (in winter) to some hours (in summer) [87]. During the day, the primary loss process is the conversion to nitric acid (HNO_3):



At nighttime, nitrate radical (NO_3) becomes important. When sunlight is present, the nitrate radical's lifetime is below one minute, but during the night, it enables another loss process for NO_2 . The resulting nitric acid is then removed from the troposphere via deposition. [9]



Nitric acid, and to some extent, nitrogen pentoxide (N_2O_5) function as reservoir for nitrogen oxides. Nitrogen pentoxide is strongly involved in the NO_x diurnal cycle because it forms during nighttime and slowly dissociates during the day, releasing the NO_x again, see reaction 2.8 to 2.10. [9, 77, 83]



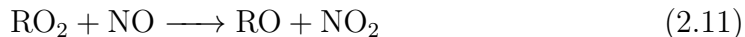
2.1.2 Volatile organic compounds

The second precursor influencing the formation of ground-level ozone is the group of volatile organic compounds (VOCs) and carbon monoxide (CO). The name VOCs describes an ensemble of gaseous organic species. Their emissions result from biogenic sources, industrial processes, and combustion. VOCs are primarily released as hydrocarbons (C_xH_y). [9]

In the atmosphere, these VOCs are successively oxidized to carbon dioxide (CO_2).

Generally, VOCs have short lifetimes (e.g. Isoprene: 60 min [9]), with methane (CH_4) posing an exception. Methane has the longest lifetime, with approximately 10 years against the reaction with the hydroxyl radical (OH). The primary sink for VOCs is the oxidation by the hydroxyl radical. For specific VOCs, other oxidants like NO_3 , O_3 , or halogen atoms play a role in the removal as well. [9]

Following the oxidation by OH , the produced organic peroxy radicals (RO_2) may follow two potential paths. The first one, reaction 2.11, is relevant for the production of ozone, and the second one, reaction 2.12, leads to the scavenging of HO_x radicals. Which reaction dominates, depends on the concentrations of NO and HO_2 . In a high- NO_x regime, reaction 2.11 takes place, and in a low- NO_x regime, reaction 2.12 takes over. [9]

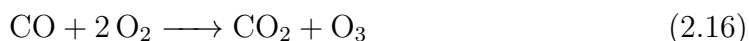
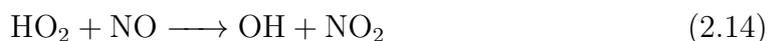
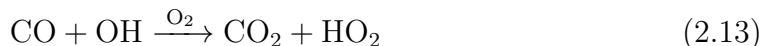


2.1.3 Carbon monoxide

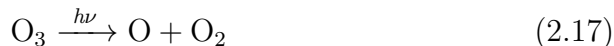
The last precursor, linked to VOCs, is carbon monoxide (CO). It forms as an important intermediate product in the oxidation of VOC to CO_2 . It is released by incomplete combustion, which is largely the case for open fires, e.g. forest fires and has a lifetime of two months, which allows for intercontinental transport, enabling the usage of CO as a tracer for combustion plumes. [9]

2.1.4 Tropospheric ozone

Tropospheric ozone is formed as a byproduct of the oxidation of VOCs and CO in the presence of NO_x . The first reaction in the process describes the oxidation of CO to CO_2 , during which HO_2 is formed (reaction 2.13). The latter reacts with NO to form NO_2 (reaction 2.14), which is photolyzed afterward (reaction 2.15). The net reaction 2.16, displays the formed ozone. It shows that NO_x is needed for the formation of O_3 but it does not deplete, contrary to VOCs, which are oxidized. This sequence of reactions provides the dominant source of ozone in the troposphere. [9]



The lifetime of ozone varies from a few days, close to the surface, to months in the dry upper troposphere [9]. The main loss process is the photolysis in the presence of water vapor, shown in reactions 2.17 & 2.18. Additional reactions with HO_x radicals can occur, see reactions 2.19 & 2.20. [9]



Ozone production relies on sufficient concentrations of NO_x, VOCs and CO. It is possible to distinguish between two regimes for ozone production. The NO_x-limited regime refers to the region where the ozone production increases with increasing concentration of NO_x, found in the bottom right of Figure 2.1. Here, reaction 2.14 competes for peroxy radicals (HO₂) with the HO_x sinks and therefore, the production of ozone only depends on the concentration of NO_x. This situation is common downwind of urban/suburban areas and in remote areas. [9]

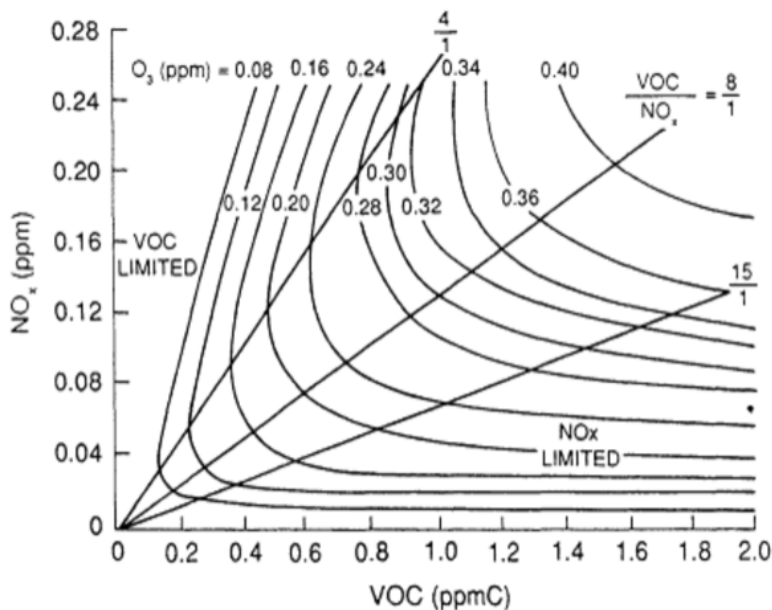


Figure 2.1: Ozone isopleths (equal mixing ratio) depending on NO_x and VOC concentration based on box model calculations. Adapted from Dodge [24] as cited in National Research Council [65].

The VOC-limited regime, on the other hand, describes a situation where ozone production increases with increasing concentrations of VOCs. Increasing the NO_x concentrations, however, decreases ozone formation. In this regime, to the left of Figure 2.1, NO_x concentrations are high, leading to HO₂ becoming the primary sink

for HO_x (reaction 2.4). Now reaction 2.4 & 2.13 compete for OH. With an increasing VOC concentration, reaction 2.13 is taking place more often leading to increased ozone concentrations. Regions, where this regime is an accurate representation, are usually located in highly polluted urban areas. [9]

2.2 Experimental foundations

In this study, a spectroscopic remote sensing technique is used to estimate emissions. During the measurements, light originating from the sun passes the atmosphere to the measurement device. On its way, different physical processes act on the radiation and lead to the observed spectrum at the surface.

The first process is scattering, which depends on the particle size in each situation. For scattering objects exceeding the wavelength of the light ($d \gg \lambda$), diffraction can be neglected and scattering is described by geometric optics. Here light rays, depicted by straight lines, do not influence each other, and their interaction with matter is described by the laws of reflection and refraction [22]. For particle sizes smaller than the wavelength of the light ($d \ll \lambda$), like atoms or molecules, scattering is described via Rayleigh scattering. The scattering cross-section shows a relatively strong wavelength dependence ($\sigma \propto \lambda^{-4}$) [86]. For particle sizes similar to the wavelength ($d \approx \lambda$), like water droplets or aerosols, Mie scattering occurs. It differs from Rayleigh scattering by favoring forward scattering and by only having a weak wavelength dependence ($\sigma \propto \lambda^{-\kappa}$ with $\kappa \in [0.5, 2.0]$) [86].

Secondly, atomic or molecular absorption processes can occur. They are based on changes in the internal state, which is quantized [23]. This means that only photons with certain energy levels are able to interact with the respective atom or molecule, which leads to particle-specific cross-sections. In reality, multiple internal transitions are possible with different probabilities, which enables the absorption of light with a broad wavelength range by chaining different transitions. For molecules, additional rotational and vibrational transitions are present, representing different energy states of relative motion of the atoms in a molecule. They absorb a different range of energy, and their combination (following selection rules) may result in continuous and complex absorption bands. [42]

The absorption by trace gases in the atmosphere is shown in Figure 2.2, where the black curve represents the ideal spectrum of a blackbody with the sun's temperature. The yellow spectrum represents the actual solar spectrum at the top of the atmosphere, and the red spectrum depicts how the spectrum is received at the surface. Furthermore, the absorption bands of some species are noted. The difference

between the spectrum at the surface and the top of the atmosphere enables conclusions about the atmospheric composition with the help of spectroscopic methods. It has to be noted, that the shown spectrum has a low spectral resolution. Zooming into specific wavelength ranges would reveal multiple Fraunhofer lines and other discrete structures, originating from molecular absorption.

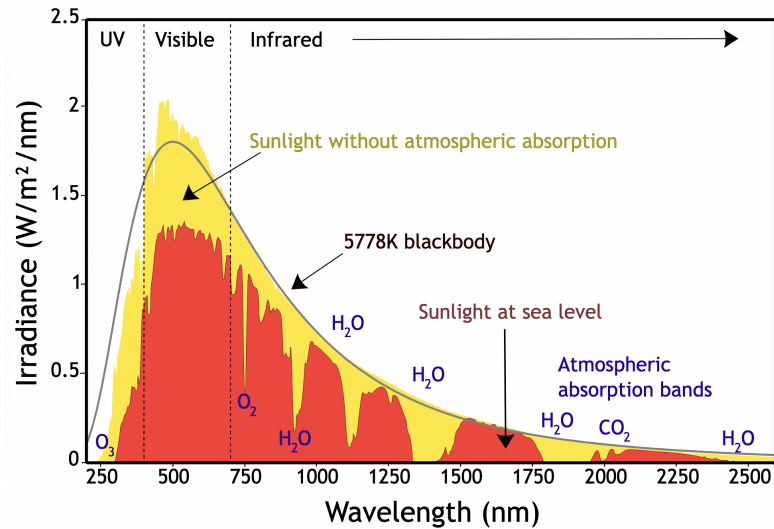


Figure 2.2: Spectrum of solar radiation at the top of the atmosphere and at the surface. Adapted from Robert A. Rohde, CC-BY-SA 3.0, https://commons.wikimedia.org/wiki/File:Solar_spectrum_en.svg

Using spectroscopic methods for the analysis of our environment is an established approach. The first studies are noted down as early as 1879 from Cornu [17]. The optical remote sensing technique applied in this work, Differential Optical Absorption Spectroscopy (DOAS), is utilized to analyze atmospheric trace gases, which absorb in the ultraviolet and visible wavelength range. [73]

The method can be subdivided into active and passive DOAS. For active DOAS, the light source is artificial. Different light sources can be used, such as lamps [46] or lasers [1]. Passive DOAS, used in this study, analyses the spectrums from natural light sources, most often the sun. It benefits from a simple experimental setup; however, the path of the light is usually not known in detail [86].

On its path through the atmosphere, it is scattered and/or absorbed by particles along the light path, as described earlier. Afterward, photons enter the ground-based telescope opening. Via a quartz fiber, the photons are directed into a spectrometer. On the inside, a blazed grating separates the light rays into their wavelengths, and the photons are collected with a charge-coupled device (CCD). Each row of pixels of the CCD aligns with a specific mean wavelength. [3, 73]

The Lambert-Beer law is used as the starting point for retrieving the trace gas

concentrations. It describes how the intensity of light changes while propagating through a medium:

$$I(\lambda, s) = I_0(\lambda) \cdot \exp\left(-\int_0^s n(s') \cdot \sigma(\lambda, s') \cdot ds'\right). \quad (2.21)$$

Here n describes the number density of the medium along the light path s' , σ describes the cross section for every wavelength, and I_0, I stand for the original and respective intensity of the light after passing the distance s inside of the medium.

The scattering by different particles is described by either Mie scattering or Rayleigh scattering. Accounting for multiple absorbers (sum over i) and the two elastic scattering mechanisms (sum over j), the Lambert-Beer law transforms into:

$$I = I_0 \cdot \exp\left(-\int_0^s \left[\sum_i^N n_i(s') \cdot \sigma_i(\lambda, s') + \sum_{j=\text{ray,mie}} n_j(s') \cdot \sigma_j(\lambda, s')\right] ds'\right). \quad (2.22)$$

Assuming that the cross sections are independent of the light path allows moving them out of the integral. This assumption is reasonable because trace gases are often located in layers. So the temperature dependence on the cross-section can be neglected. [86] This yields:

$$I = I_0 \cdot \exp\left(-\sum_i^N \sigma_i(\lambda) \cdot \int_0^s n_i(s') \cdot ds' - \sum_{j=\text{ray,mie}} \sigma_j(\lambda) \int_0^s n_j(s') \cdot ds'\right) \quad (2.23)$$

$$= I_0 \cdot \exp\left(-\sum_i^N \sigma_i(\lambda) \cdot \text{SCD}_i - \sum_{j=\text{ray,mie}} \sigma_j(\lambda) \cdot \text{SCD}_j\right). \quad (2.24)$$

In equation 2.24 the slant column density is introduced, defined as the following:

$$\text{SCD} = \int n(s) \cdot ds. \quad (2.25)$$

SCD is the quantity of interest and describes the concentration of an absorber along the mean light path (s), see Figure 2.3. In reality, there are a lot of different light paths due to the stochastic nature of scattering. Furthermore, multiple scattering processes occur. These processes are indirectly incorporated into the slant column density by integrating along the light path.

The DOAS method distinguishes between a slow and a fast-changing fraction of the cross-section concerning the wavelength. The low-frequency part of the cross-section $\tilde{\sigma}$ accounts for broadband absorption and can be approximated by a polynomial ($\sum_p c'_p \lambda^p$). The high-frequency part of the cross-section, the differential cross-section σ' , only includes the absorber-specific narrow band absorption, which is used to

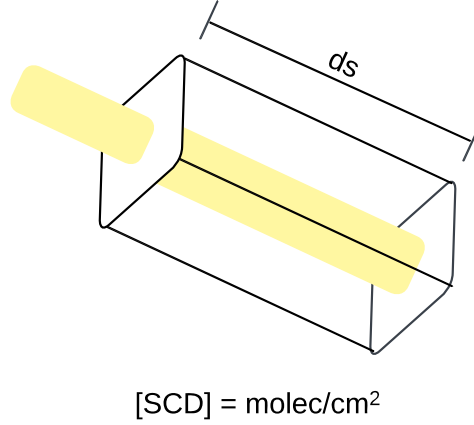


Figure 2.3: The slant column density describes the number density of a pollutant integrated along the mean lightpath, here shown in yellow. A common integral range is from the top of the atmosphere to the surface. The light path orientation depends on the used platform.

retrieve the slant column densities. [86]

$$\sigma' = \sigma - \tilde{\sigma} = \sigma - \sum_p c'_p \lambda^p \quad (2.26)$$

The elastic scattering by Mie and Rayleigh can be fitted by a polynomial too, due to their wavelength dependence (Ray $\propto \lambda^{-4}$, Mie $\propto \lambda^{-\kappa}$, $\kappa \in [0.5, 2.0]$). For simplicity, only one combined polynomial ($\sum_p c_p \lambda^p$) is denoted.

$$I = I_0 \cdot \exp \left(- \sum_i^N \text{SCD}_i \cdot \sigma'_i(\lambda) - \sum_p c_p \lambda^p \right) \quad (2.27)$$

Taking the natural logarithm and reordering the equation to the optical depth τ leads to the DOAS equation:

$$\tau = \ln \left(\frac{I_0}{I} \right) = \sum_i^N \text{SCD}_i \cdot \sigma'_i(\lambda) + \sum_p c_p \lambda^p. \quad (2.28)$$

This linear equation connects the measured quantity τ with the slant column densities. Multiplicative effects on I or I_0 cancel out due to the division. This reduces the effort to calibrate the spectrums if both are taken close in time from the same device. This equation holds for every wavelength. Usually, the wavelength window is selected in a way that the system of equations is overdetermined. Finally, a least-squares fit can be used to obtain the needed quantities: SCD and c_p . [86]

The quality of the fit can be derived from the residual of the optical depths, given via

$$r_k = \tau_{\text{meas}}(\lambda_k) - \tau_{\text{fit}}(\lambda_k). \quad (2.29)$$

All properties of the spectrum, which are not described by the fit, are located in the residual. The root mean square (RMS) from all N wavelengths of the fit window determines the quality of the DOAS fit, where m denotes the number of fit parameters.

$$\text{RMS} = \sqrt{\frac{1}{N - m} \sum_k^N r_k^2}. \quad (2.30)$$

Note that the resolution of the differential cross-section is usually higher than the measured spectrum of the device. If it is not corrected, it will lead to bad fits due to the different widths of the absorption lines. The cross sections are matched to the coarser resolution of the device by convoluting the cross sections with the slit function of the measurement device. [77]

The DOAS method developed over time, and more and more trace gases became detectable and analyzable with DOAS [77, 90]. Furthermore, different setups have been developed and used: Ground-based DOAS [85], car-DOAS [49], satellite-based DOAS [78] and airplane-based DOAS [82].

2.3 Modeling foundations

Brasseur and Jacob [9] state that using models to gain knowledge is a novel third option of the scientific procedure. In their opinion, it complements theoretical reasoning and experimental methods.

”A model is a simplified representation of a complex system that enables inference of the behaviour of that system.”

This quote² from Brasseur and Jacob [9] in their book *Modeling of Atmospheric Chemistry* summarizes well the purpose and general definition. It highlights the key points of a model, serving as a simplification of the original system while preserving the main properties to infer new conclusions.

Many different model types and purposes are relevant in modern science, e.g., mathematical models, cognitive models, statistical models and laboratory models [9]. This study focuses on numerical models, specifically numerical weather prediction (NWP) and chemical models.

The first mathematical ideas concerning meteorological models were written down by Cleveland Abbe in 1901, followed by Vilhelm Bjerknes in 1904. Later, Bjerknes suggested that the meteorological variables pressure, temperature, wind vector, air

²Brasseur, G. P. and Jacob, D. J. “Modeling of Atmospheric Chemistry”. Cambridge University Press, (2017). DOI: 10.1017/9781316544754, page 2.

density, water vapor content and their time-evolution could be predicted by seven basic equations [7].

The first implementation of weather prediction, a hindcast, in a computer was done in Princeton in 1959. It was possible due to the introduction of approximations for large-scale motion. Four years later the first real-time forecast was simulated in Stockholm. In the 1970s, supercomputing power became available. It led to the first solvers, which were able to solve the full set of equations of Abbe and Bjerknes. [5]

These equations take a different shape depending on the frame of reference. The Lagrangian approach uses a moving frame of reference, which follows the atmospheric flow. There are various types of Lagrangian models, which account for the processes of turbulence and wind shear on air parcels differently; mean trajectories, box models, Gaussian puffs, and Lagrangian particle dispersion models (LPDM) are the most commonly used types, out of which LPDMs are the most sophisticated and computationally expensive. The latter generate numerous particles, representing air parcels, with small random deviations in their velocities, which are dispersed over the model domain depending on the wind field. This approach has several advantages: trajectories of particles are available, mixing in the atmosphere is better described, and the integration of the Lagrangian equations is numerically stable. However, it relies on an externally generated wind field, most often done via an Eulerian model. [9, 58]

The Eulerian approach generates a fixed geographical grid and calculates all quantities in every grid cell. This approach enables having a well-defined concentration field over the whole domain. Nonlinear chemistry and mass conservation are captured better than in Lagrangian models. Lastly, comparing observations is more straightforward because stations are usually at a fixed location. [9]

The equations of Abbe and Bjerknes describe the core of meteorological modeling in the following described for an Eulerian frame of reference. The first one, equation 2.31 describes the conservation of air mass in a compressible flow. It states that any change of the air density (ρ_a) in time has to be compensated by the spatial change of the air density multiplied by the wind field \vec{v} . [9]

$$\underbrace{\frac{\partial \rho_a}{\partial t}}_{\text{temporal change}} + \underbrace{\vec{\nabla}(\rho_a \cdot \vec{v})}_{\text{spatial change}} = 0 \quad (2.31)$$

The continuity equation for the mass mixing ratio of water vapor (μ) is similar to equation 2.31. Two additional terms on the right-hand side describe the production rates (P) and the loss rates (L) of water vapor [9], e.g., evaporation and

condensation.

$$\frac{\partial(\rho_a \mu)}{\partial t} + \vec{\nabla}(\rho_a \cdot \mu \cdot \vec{v}) = \rho_a (P_{\text{H}_2\text{O}} - L_{\text{H}_2\text{O}}). \quad (2.32)$$

The third equation Bjerknes mentions is the conservation of energy, for which it is useful to introduce the quantity potential temperature (Θ):

$$\Theta = T \left(\frac{p_0}{p} \right)^{\frac{R}{c_p}}. \quad (2.33)$$

Here R denotes the gas constant, T the temperature, and c_p the specific heat at constant pressure. The potential temperature describes the temperature an air parcel would have if brought adiabatically from pressure (p) to the reference pressure (p_0). In an adiabatic environment, the potential temperature is conserved with altitude. [9]

The energy balance of an air parcel can be changed, following the first law of thermodynamics, either by changing the internal energy or by inducing work by expansion. By introducing loss processes, the diabatic heating term (Q) has to be considered. After some rearrangements, the first law of thermodynamics takes the shape of

$$\frac{d\Theta}{dt} = \left(\frac{p_0}{p} \right)^{\frac{R}{c_p}} \frac{Q}{c_p}. \quad (2.34)$$

It is visible that if there are no diabatic processes present ($Q = 0$) the potential temperature is a conserved quantity in time. Hence, it can be interpreted as a measure of the heat content of an air parcel. Changes in temperature via radiative interaction are considered in the net heating rate Q . Depending on altitude, different effects influence the local energy budget and have to be incorporated. [9]

The last conservation equation is the conservation of momentum, the Navier-Stokes equation. Here it is noted down for a rotating frame of reference:

$$\frac{\partial \vec{v}}{\partial t} + (\vec{v} \cdot \nabla) \vec{v} = \underbrace{-2(\vec{\Omega} \times \vec{v})}_{\text{Coriolis}} + \underbrace{\Omega^2 \vec{R}}_{\text{centripetal}} - \frac{1}{\rho_a} \nabla p + \vec{g}. \quad (2.35)$$

$\vec{\Omega}$ denotes the angular velocity of Earth, and \vec{R} represents the position vector perpendicular to the Earth's axis of rotation. Hence, the change of velocity, $\frac{\partial \vec{v}}{\partial t}$, depends on the Coriolis acceleration, the centripetal acceleration, the pressure gradient, ∇p , and the gravitational acceleration (\vec{g}). [9]

For linking the pressure and the temperature Bjerknes cites the ideal gas law. The atmospheric pressure is low enough to be sufficient as a description of the atmo-

sphere, where M_a represents the molar mass of air. [9]

$$p \cdot M_a = \rho_a \cdot R \cdot T. \quad (2.36)$$

State-of-the-art NWP models solve these seven equations at a given spatial and temporal resolution in the dynamical core. This creates a distinct separation between resolved and unresolved features, depending on their scale of motion. Unresolved processes are incorporated into the model via source terms, and their influence on the resolved scales is parameterized. [5]

The chemical models either solve the meteorological equations simultaneously, commonly referred to as "online atmospheric chemical models", or use meteorological data from another model (offline atmospheric chemical models). The advantages of online models are that they fully couple chemical transport with the dynamic core. This is more realistic because chemistry and meteorology affect each other, e.g., aerosols serve as cloud condensation nuclei [70] and clouds influence chemical transformations [57]. Further advantages are that they do not need high-resolution meteorological archives and are more precise due to detailed meteorological variables present at runtime. However, the operation and interpretation of online models are more complex. [9]

For chemical models, the continuity equation has to be solved for each species.

$$\frac{\partial C_i}{\partial t} + \vec{v} \cdot \vec{\nabla} C_i = P_i(C_i) - L_i(C_i) \quad (2.37)$$

This equation embodies the conservation of mass for the i -th species of an ensemble. It is denoted for the mixing ratios C_i . Apart from deposition and emission processes, the contributions from chemical reactions and interconversion are found in the production and loss rates. The computational cost of an ensemble of coupled chemical compounds is often larger than the computational cost of the meteorological simulation. [9]

Due to the chaotic nature of the problem of meteorological forecasts, non-perfect knowledge of the starting conditions leads to deviating model output. This is the case for free-running models, which generate an ensemble of possible atmospheric states. To reduce the chaotic behavior, data assimilation can be applied, which nudges the model to observed values, and can therefore recreate an observed atmospheric state [9]. Spectral nudging specifically forces the model to satisfy large-scale flow conditions inside the simulated domains together with the constraints from the boundary conditions [62, 94, 106].

To ensure that the model output is realistic, a spin-up period has to be considered while choosing the simulation period. The model is initialized with input data, which is not in equilibrium. The spin-up period is defined as the needed time for the simulated atmospheric state to reach equilibrium concerning the chemical mechanisms, emissions, and meteorological conditions. The duration of the spin-up depends on how far the initial state of the model deviates from the equilibrium state, which is influenced by several variables, e.g., the quality of the model input fields [53] or the lifetime of the studied chemical species. [9]

When evaluating model output, several error sources have to be considered. In general, the question is whether the error of the model diminishes its usefulness, not whether there an error is present. Modeling errors can reside in

1. uncertainties in input data
2. unsuitable assumptions/configuration
3. incomplete implementations
4. imperfect scientific understanding.

The 4th point is especially interesting because it reveals where the current understanding can be improved. However, in practice, it is not always easy to identify the error source.

Chapter 3

Methodology

3.1 Previous work

DOAS is often used in a mobile setup to allow for flexibility. In this study, DOAS measurements are conducted by bicycle, whereas a commonly applied method in literature is DOAS measurements by car (car DOAS). Schreier, Richter, and Burrows [83] combined mobile zenith-sky DOAS measurements with tower DOAS measurements to gain interesting insights into the spatiotemporal NO_2 distribution over Vienna. Estimations of emissions by car DOAS measurements are conducted among others by Johansson et al. [51] for Beijing, by Shaiganfar et al. [88] for Delhi and Ibrahim et al. [49] for Mannheim and Ludwigshafen. Out of the before-named authors, Schreier, Richter, and Burrows [83] and Johansson et al. [51] use the zenith-sky setup, whereas the others use the Multi-Axis DOAS (MAX-DOAS), see Wittrock et al. [108] for further details on MAX-DOAS.

WRF-Chem is used in a wide range of applications. It is used for global-scale analysis, e.g., transpacific transport, see Hu et al. [47]. Relevant case studies of regional domains are conducted as well, among others, by Georgiou et al. [34] for Cyprus and Tie et al. [98] for Mexico City. Tie et al. [98] studied the species O_3 , NO_x and CO and compared the model output with surface stations. They obtain a good agreement with the diurnal variations. With the help of sensitivity studies, they conclude that the O_3 diurnal variations are due to chemical transformations, whereas the diurnal variations for NO_x and CO are due to changes in the height of the planetary boundary layer as well as changes in emissions. Georgiou et al. [34], on the other hand, studied summertime air pollution over the eastern Mediterranean, focus on Cyprus. The authors compare their model results with an observational network and found that the ozone concentrations are overestimated. Additionally,

they are not able to capture the diurnal variability of precursors of ozone, which they attribute to the missing representation of local NO_x emissions in the anthropogenic emission inventory.

FLEXPART-WRF is applied for transport modeling. Cécé et al. [15] coupled it with large eddy simulations and investigated the dispersion of anthropogenic NO_x on tropical islands. Their forward simulation of a power plant plume agreed well with the nocturnal observations. The authors concluded, that a high-resolution grid (< 1 km) is required to simulate air quality over complex terrain accurately. Another approach is used by Lee et al. [56]. They analyze the transport of NO_x in East Asia. Next to satellite and in situ measurements, FLEXPART-WRF was run backward to track the important emission sources for Wuhan in China. The authors found that the decrease in $\text{PM}_{2.5}$ during the COVID-19 lockdown was the consequence of two factors: 80 % of the decrease can be attributed to the decrease of emissions in surrounding areas, and the residual 20 % originated from meteorological changes.

As established, a combination of DOAS and numerical modeling is a commonly used and well-proven methodology when studying the emission and transport of pollutants in regional modeling (mainly WRF-chem; Georgiou et al. [34] and Tie et al. [98]) or in the case of sole source (FLEXPART-WRF; Cécé et al. [15]). Here, we combine all three components in a novel way to get an in-depth understanding of emission source characterization over Bremen. The DOAS measurements and the emission calculation are similar to the ones from Ibrahim et al. [49]. Afterward, a regional WRF-Chem model, centered at Bremen, is run to retrieve the full atmospheric state, which is then compared against the output of a forward FLEXPART-WRF to evaluate the impact of the local waste incineration plant as a NO_x source.

3.2 Bicycle DOAS measurements

This work uses bicycle DOAS measurements in a zenith-sky setup. That has the advantage of being insensitive to deviations in orientation. This feature is even more important when conducting measurements using a bicycle compared to using a car. In zenith-sky mode, an elevation angle of 90° is used [83]. Furthermore, the retrieval is rather straightforward compared to MAX-DOAS, where the relative azimuth angle influences the air mass factor (AMF), which adds another layer of complexity [83]. Additionally, fewer obstacles are present in the light path compared to a lower elevation. However, measurements in zenith-sky mode have a lower sensitivity compared to off-axis measurements. [83]

The hardware used in this study is depicted in Figure 3.1. It consists of a GPS



Figure 3.1: The components of the setup. a) shows a GPS receiver, b) charging cable for the computer, c) USB lamp, d) power bank, e) Avantes, f) USB data connection between Avantes and computer, h) laptop, and g) bicycle bag or pannier.

receiver (a), a USB-controllable lamp (c), a power bank and its cable (b+d), the Avantes spectrometer, the optical fiber and the telescope opening (e). A data cable (f) from the spectrometer to the computer (h), in addition to a pannier (g), is used.

The measurement device is an AvaSpec-ULS2048x64 spectrometer, in short, Avantes, the same device used by Schreier, Richter, and Burrows [83]. Its dimensions are 175 x 110 x 44 mm. It is robust and light in weight with its 855 g. Spectral measurements between 290 nm and 550 nm are possible with a spectral resolution of 0.65 nm [83]. For the bicycle DOAS application, its weight and portability were the important selection criteria.

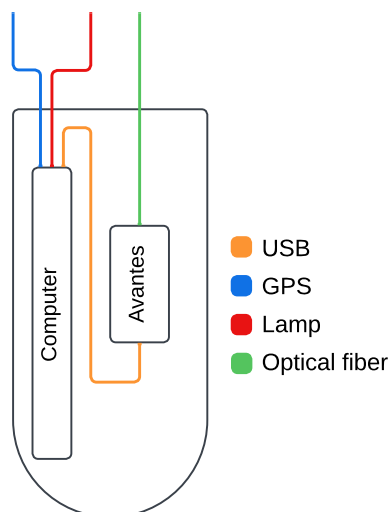


Figure 3.2: A sketch of the setup of the bag and the cable layout. The Avantes is vertically aligned, and the computer slides behind it. With the help of clothing as cushioning, the devices were fixed in place, and all cables maintained a minimum curvature.

In Figure 3.2 the setup of the bag is shown. The spectrometer is vertically placed inside the bag. The measurement computer is placed next to it. The design enables using the laptop during tours without moving the spectrometer and the optical fiber. Furthermore, clothes and towels are used to dampen the vibrations and keep everything in place. At the bottom, two towels are used to maintain a minimum curvature of the USB data cable at the back of the Avantes.

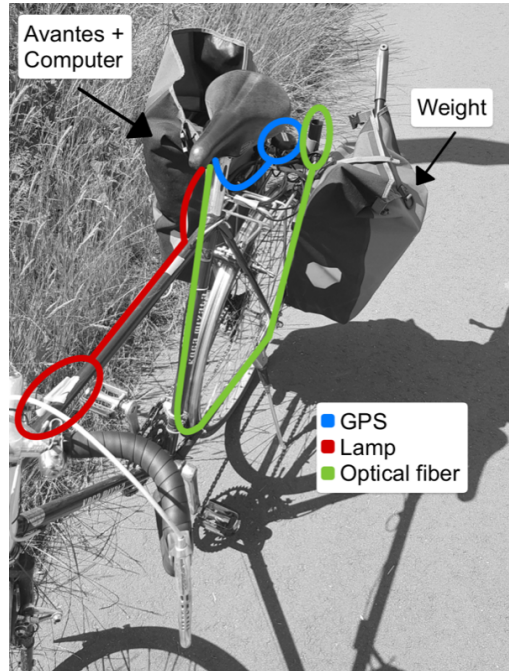


Figure 3.3: The setup of the bicycle. One bag contains the Avantes and the laptop, whereas the other only contains weight to balance the movement. The USB lamp (red) is attached close to the handlebar. The GPS receiver (blue) and the optical fiber (green) are fixed to the back of the bicycle. The curvature is not allowed to fall below a certain threshold for the optical fiber, which is why the installation takes a detour to the pedals.

Figure 3.3 depicts how the Avantes is attached to the bicycle. It is placed inside the bag on one side. The optical fiber leaves the bag towards the front and follows a semicircle to the telescope opening at the back. The GPS receiver is located right next to the telescope opening. Furthermore, one small lamp is placed at the front, close to the handlebar. On one side, it indicates whether a GPS signal is present. On the other side, it flashes green when a measurement is saved to the disk.

The optical fiber is fixed close to the pedals to avoid accidentally entangling them while riding the bicycle. Additionally, another bag is used on the other side of the Avantes. Its sole purpose is to counterbalance so that the deviations from the 90° viewing angle of the telescope are minimized.

3.2.1 Bicycle DOAS routes

Here the same procedure as in Ibrahim et al. [49] is applied. Briefly, the emission source is encircled by DOAS-bicycle measurements. Combining the inherent vertical integration along the light path for the SCDs with a horizontal integration along the driving path allows calculating the flux of molecules through the spanned area by the driving route and the vertical direction. This enables comparing the trace gas fluxes at the influx region and the outflux region depending on the wind direction that ideally leads to an elevated signal downwind of the source, see Figure 3.4. The detailed implementation and the mathematical formulation are found below in Section 3.4. [49]

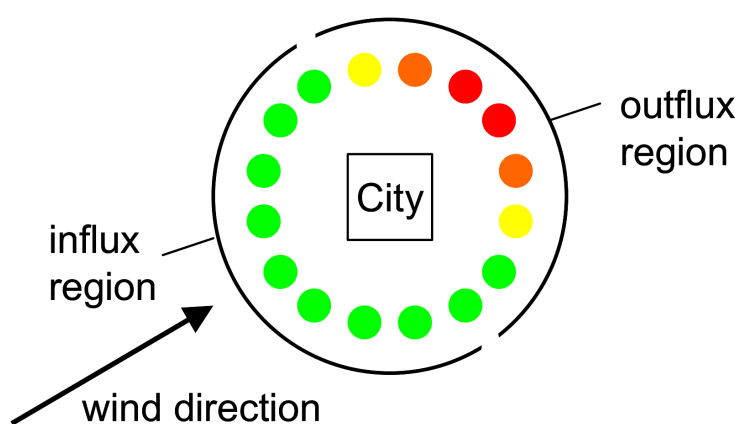


Figure 3.4: Schematic representation of calculating emissions of a source using the Gauss Theorem, adapted from Ibrahim et al. [49]. The source is encircled with the DOAS measurements, here depicted as a city. Due to a constant wind field, the background signal is found in the influx region. The signal in the outflux region consists of the background signal plus the emission of the source. The difference between the outflux and influx region is used to calculate the emission.

The first emission source studied is the waste incineration plant of the local electricity provider swb. It is located at the edge of the northern side of the city (Figure 3.5). At the facility, waste from residents, residual sludge and industrial waste is burned for electricity generation. Additionally, the power plant is coupled to district heating. In total, the plant can generate 270 000 MW h of electricity and 200 000 MW h of heat. Further technical information can be found on the website of swb [95].

The selected measurement route around the incineration facility is approximately 10 km long (Figure 3.5). An agricultural area, the Blockland, is located on the northern side of the plant. On the southern side, the route crosses highway A27, and leads through allotments.

The second emission source studied is the airport of Bremen. It is located in the south of Bremen. Approximately 2 500 000 passengers are transported annually, with

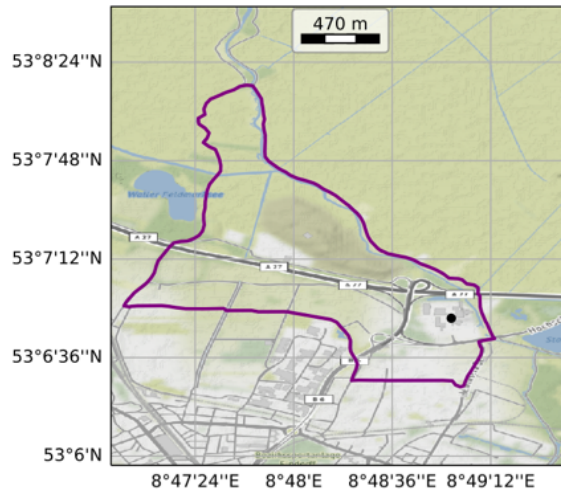


Figure 3.5: The route around the waste incineration plant, approximately 10 km long. The facility is marked with a black dot. Agriculturally used land is found in the north and the city is located toward the south.

40 000 arrivals and departures at the airport. In total, 500 companies and 16 000 employees are settled in the area known as "Airport City" around the airport. [10]

The airport is almost encircled by the city, except in the southwest direction (Figure 3.6). In the northeast part, trees obstruct zenith-sky measurements. One round is approximately 12 km long. Compared with the waste incineration plant, the airport represents a different source, as emissions depend on air traffic and are not localized to one spot (chimney).

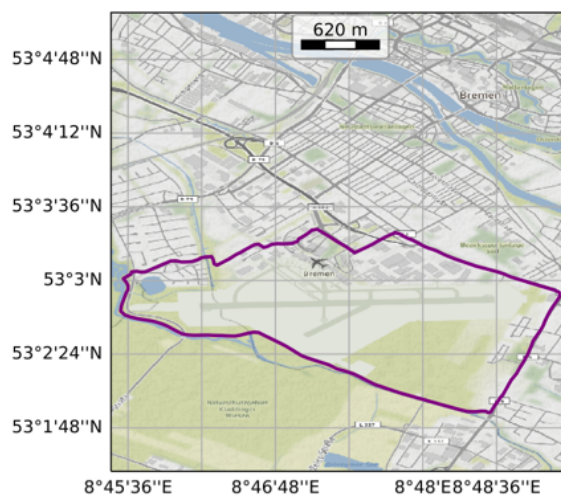


Figure 3.6: Route around the airport, approx. 12 km. Only towards the southwest rural land is found. All other sides merge with the city of Bremen.

3.2.2 Measurement setup with two Avantes

As the airport route was considerably long (≈ 60 minutes), it risked breaking the assumption of stable atmospheric conditions during the observation. With this in mind, on 23.06.2022, a second Avantes was used to test the sensitivity of the observations to the time required to complete a full circle. The above-described setup was just duplicated. Having a second Avantes enables splitting the route in half. One Avantes is moved through the inflow region and the other through the outflow region. This results in twice the amount of rounds per measurement period.

To compare the performance, the two devices measured simultaneously at the same location with the same alignment over 10 minutes. Afterward, the mean offset is used to correct the second Avantes. The offset is motivated by the DOAS equation, where differences in I_0 lead to an offset in the slant column densities. The offset was calculated to be 6.52×10^{14} molec cm^{-2} . In Figure 3.7 the differential slant columns measured by the two Avantes are depicted during the calibration period.

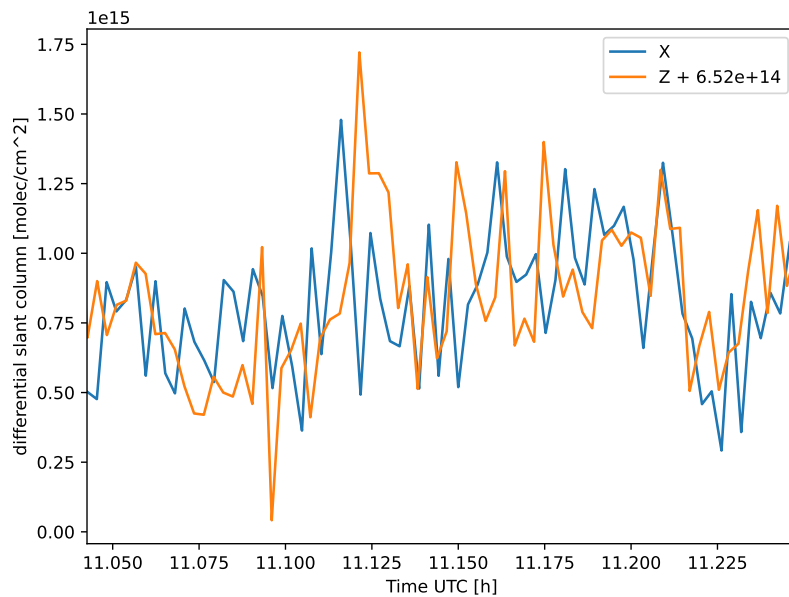


Figure 3.7: Calibration measurements at the same location during a set period to calculate the offset between both Avantes(X & Z). The offset is already applied in the Figure for the Z.

For the DOAS fit of the second device, the same settings are used. The main difference in the procedure is the device-specific slit function and a device-specific dark measurement.

3.3 DOAS data retrieval

3.3.1 DOAS retrieval software and settings

The software (AMAX-OMA) used for the retrieval is from the DOAS Group of the Institute of Environmental Physics of the University of Bremen, written by Richter [77]. The following elaboration on the fitting routine is based on the descriptions of Seyler [86].

The spectrometer settings, exposure time, GPS logging and further options are set in *AMAX-OMA*. The whole measurement process is configurable. The raw data from the CCD is read out and saved in binary format [86].

In this study, the CAR option was used to enable the logging of the GPS signal from a receiver. Additionally, the exposure time was set to automatic. [86] An integration time of 10 s is used, which relates to one spectrum every 56 m when assuming an average driving speed of 20 km h⁻¹.

After retrieving the raw data, the slit function of the device has to be determined. This is done by analyzing measurements with a HgCd lamp in the software *Resolut*. It is saved in a file for later usage. Before performing the actual fit, the spectra have to be preprocessed. This is taken care of by *NPrepare*. It subtracts the dark measurements and removes spectra with a low number of counts. Furthermore, it applies a wavelength calibration with the help of the spectrum of the HgCd lamp. [86]

NLIND uses the processed files and applies a high-resolution wavelength calibration with the help of Fraunhofer atlas of Kurucz et al. [54]. Furthermore, it prepares the cross-sections by convolution with the before-calculated slit functions. Afterward, the main fitting algorithm is run. The intensities are aligned, allowing for shifts and squeezes. The shift and squeeze parameters are obtained by a nonlinear Levenberg-Marquardt fit. During every step of the fit, a linear least square fit is applied to retrieve the slant column densities. This procedure is repeated until convergence is reached. [86]

Fitting settings are similar to Schreier, Richter, and Burrows [83], see Table 3.1. The background reference spectrum is taken from 23 June 2022 at a solar zenith angle (SZA) of 30.45° for all measurements.

Table 3.1: Fitting settings used in this study, similar to Schreier, Richter, and Burrows [83].

Fit parameter		Selection/source
Spectral range		425 nm - 490 nm
Polynomial degree		6
Wavelength calibration		Solar atlas [54]
Reference		23 June 2022, SZA = 30.45°
Cross-section	Temperature	Data source
O ₃	223 K	Serdyuchenko et al. [84] with I_0 corr.
NO ₂	298 K	Vandaele et al. [105] with I_0 correction
O ₄	293 K	Thalman and Volkamer [97]
H ₂ O	-	Rozaanov et al. [79]
Ring	-	QDOAS [20]

3.3.2 Calculation of vertical column densities

The retrieved slant column densities are a difficult quantity to compare among different measurement campaigns because they depend on the light path, see equation 2.25. That, however, is not known in detail for passive DOAS. For this reason, the slant column densities are converted into vertical column densities, defined via:

$$\text{VCD} = \int n(z) \cdot dz. \quad (3.1)$$

For the VCD the number density is integrated along the altitude and is independent of the actual mean light path.

Since the emissions are located in the troposphere, further discussions on vertical column densities are concentrated on tropospheric vertical column densities. Removing the stratospheric signal is done by applying a correction (for details, see 3.3.3). In the following chapters, *vertical column* will be used instead of *tropospheric vertical column density* for brevity.

The two tropospheric quantities are linked via the air mass factor

$$\text{VCD}^{\text{trop}} = \frac{\text{SCD}^{\text{trop}}}{\text{AMF}^{\text{trop}}}. \quad (3.2)$$

The AMF considers the viewing geometry, aerosol distribution, and pollutants profiles among other parameters [73]. For the zenith-sky mode, it is possible to use a geometrical approximation for the tropospheric AMF, which results in an AMF of 1. In this work, we use a tropospheric AMF of 1.3. Radiative transfer model (SCIA-TRAN [79]) calculations showed that this value is more realistic than the geometric value [83] by accounting for, among others, multiple scattering and aerosols.

3.3.3 Stratospheric correction

When measuring over a long period of the day, the diurnal cycle of NO_2 in the stratosphere has to be considered. During the night, NO_2 converts to the reservoir N_2O_5 , see reaction 2.6. During the day, N_2O_5 is photolyzed back via reaction 2.9, so the vertical column density of NO_2 in the stratosphere is steadily increasing. Because the retrieved slant column density is integrated along the whole optical path (stratosphere and troposphere), it also increases during the day. Furthermore, the stratospheric AMF varies strongly with the changing SZA. Because both processes perturb the analysis of the tropospheric concentrations, the stratospheric slant column density is removed from the analysis.

Subtracting the stratospheric slant column density from the total slant column density yields the fraction of the slant column which is located in the troposphere:

$$\text{SCD}^{\text{trop}} = \text{SCD} - \text{SCD}^{\text{strat}}. \quad (3.3)$$

The SCD can be further divided into the differential slant column density (dSCD) of the DOAS fit and the slant column density of the reference measurement (SCD_{ref}), which again is composed of the tropospheric and stratospheric part:

$$\text{SCD}^{\text{trop}} = \text{dSCD} + \underbrace{\text{SCD}_{\text{ref}}^{\text{trop}} + \text{SCD}_{\text{ref}}^{\text{strat}}}_{\text{SCD}_{\text{ref}}} - \text{SCD}^{\text{strat}}. \quad (3.4)$$

For the tropospheric reference slant column density ($\text{SCD}_{\text{ref}}^{\text{trop}}$), a constant value of $1.5 \times 10^{15} \text{ molec m}^{-2}$ is assumed in this work. It equals the average of Popp et al. [74] and the published value for the winter from Huijnen et al. [48]. The two stratospheric terms are approximated by using the Bremen 3d chemistry transport model (B3dCTM). It combines the Bremen transport model and the Bremen two-dimensional model of the stratosphere and mesosphere, see Hilboll, Richter, and Burrows [44] for more detailed information. As the model reproduces the diurnal cycle of the stratosphere well, but the absolute values are off, results are scaled with stratospheric columns from the Tropospheric Monitoring Instrument (TROPOMI) [16] via

$$s = \frac{\text{VCD}^{\text{sat}}(t_{\text{overpass}})}{\text{VCD}^{\text{model}}(t_{\text{overpass}})} \quad (3.5)$$

where t_{overpass} is the overpass time of the satellite. The VCD^{sat} is taken from the closest TROPOMI pixel to the bicycle DOAS measurement location.

This results in the equation for the stratospheric correction

$$\begin{aligned} \text{SCD}^{\text{trop}} = & \text{dSCD} + \text{SCD}_{\text{ref}}^{\text{trop}} + \text{VCD}^{\text{model}}(t_{\text{ref}}) \cdot \text{AMF}_{\text{ref}}^{\text{strat}} \cdot s' \\ & - \text{VCD}^{\text{model}}(t) \cdot \text{AMF}^{\text{strat}} \cdot s. \end{aligned} \quad (3.6)$$

The model VCDs are converted to SCDs with stratospheric AMFs calculated by the radiative transfer model SCIATRAN [79]. Note that the measurement time and location of the reference spectrum are, in general, different from the time and location of the measurement. That means even though the last two terms look similar, they do not compensate for each other.

3.4 Calculation of emissions

The calculated vertical columns can be used to calculate the emissions of each facility based on the divergence theorem of Gauss (equation 3.7). On one side of the equation, the divergence of a vector field in a certain volume is summed up. This equals the sources and sinks of a vector field. The theorem then states that this sum is equal to the sum of the vector field along the surface of the volume. For an arbitrary vector field \vec{B} , which fulfills the requirements for the divergence theorem to hold, it is given via the following equation:

$$\int_V (\vec{\nabla} \cdot \vec{B}(\vec{x})) dV \stackrel{\text{Gauss}}{=} \int_{\partial V} \vec{B}(\vec{x}) d\vec{A}. \quad (3.7)$$

This theorem can be generalized to other dimensions. Here a two-dimensional surface instead of a volume is used. The respective vector field \vec{B} is substituted by the wind field scaled with the vertical column density.

$$\vec{B}(\vec{x}) = \text{VCD}(\vec{x}) \cdot \vec{v}(\vec{x}) \quad (3.8)$$

That substitution yields

$$\int_A (\vec{\nabla} \cdot \text{VCD}(\vec{x}) \cdot \vec{v}(\vec{x})) dA \stackrel{\text{Gauss}}{=} \int_{\partial A} \text{VCD}(\vec{x}) \cdot \vec{v}(\vec{x}) d\vec{s}. \quad (3.9)$$

The boundary of the area ∂A equals the circle around the source. Under the assumption that the wind field stays constant during one circle, the right side of equation 3.9 is simplified to

$$F_{\text{NO}_2} = \int_{\partial A} \text{VCD}(s) \cdot \vec{v} \cdot \vec{n}(s) ds \quad (3.10)$$

$$= \sum_i \text{VCD}_i(s) \cdot \vec{v} \cdot \vec{n}_i(s) \cdot \Delta s_i \quad (3.11)$$

The last equation results from taking only discrete measurements, where \vec{n} describes the normal vector at each measurement along the circle and Δs_i the distance between two successive measurements.

With the help of equation 3.11 the flux of NO_2 (F_{NO_2}) in molec s^{-1} is calculated. The scalar product between the wind field and the normal vector ensures that the signal on the incoming region has an opposite sign compared to the outgoing region. This idea is shown in Figure 3.4.

To ensure that the summation is carried out along the same path every time, the driven round is projected on an ideal path, which was chosen to be the most driven route. An example projection is shown in detail in the appendix, Figure 1a.

For the wind speed and direction, hourly values from the Deutscher Wetterdienst (DWD) [29] are used. The respective station is located next to the airport in Bremen.

To compare the calculated NO_2 flux with the published emissions, a conversion to NO_x and correction for the distance between the emission source and measurement location is necessary:

$$F_{\text{NO}_x} = c_\tau \cdot c_L \cdot F_{\text{NO}_2}. \quad (3.12)$$

Before the conversion, the flux of NO_2 in molec s^{-1} is converted to kg s^{-1} . The first factor, c_L , describes the partitioning of NO_x into NO and NO_2 . Given that most NO_x in urban plumes is emitted as NO [69], the partitioning of the plume is dependent on the time since its emission. The passed time from the emission to the DOAS measurement is influenced by various factors, e.g., plume pathway, driving route, and wind speed. Ibrahim et al. [49] used a numerical value of 1.35 for the partitioning factor evaluating Car-DOAS. Due to lacking information on the partitioning at the measuring location, this value is adopted. It represents NO_x composed of 74% NO_2 and 26% NO . The assumption of the same partitioning introduces a large uncertainty because the distance to the source using a CAR exceeds the distance while cycling.

The second correction factor c_τ considers the loss of NO_x from the emission location to the measurement location. Different lifetimes for NO_x were found, ranging from 1.5 h to 7.6 h [55, 71, 80, 81, 91]. Given the assumed partitioning of NO_x , the value of 6 h found by Beirle et al. [6] for the NO_2 lifetime based on GOME measurements over Germany is adapted for the NO_x lifetime (τ). A value of 6 h is supported by the findings of Lamsal et al. [55] and Spicer [91] for the USA.

$$c_\tau = \exp\left(\left(\frac{r}{w}\right) / \tau\right) \quad (3.13)$$

Due to the small distances to the source, the correction factor is not significantly different from 1. In equation 3.13, r denotes the distance to the source (typically several hundred meters) and w wind speed. [88]

To ensure that no measurement with incorrect input data is evaluated, two criteria are defined for filtering the total rounds. **i)** The wind direction of the database has to match the direction of plume dispersion, if visible. **ii)** The wind should not introduce a big background signal from the city.

These criteria lead to the exclusion of three out of 16 rounds for the waste incineration plant. In two of the three (Figure 2b, 2c in the appendix), the wind direction from the DWD database [29] does not match the observed wind direction. The third round (Figure 2a in the appendix) is excluded because, on that day, the wind was coming from the city. There was a high signal in the inflow region, which was not measured in the outflow region. A possible explanation is that the NO_2 was diluted over the area and was not distinguishable from the background when leaving the area. Another possibility might be, that the atmosphere was not stable during that round. Thus, the air parcel with a high concentration was measured in the inflow region but missed in the outflow region.

3.4.1 Propagation of uncertainty

The quantities in the stratospheric correction (equation 3.6) have an uncertainty attached to them. The propagation of uncertainty for the corrected tropospheric slant column is given via:

$$\begin{aligned} \delta\text{SCD}^{\text{trop}} = & [(1 \cdot \delta\text{dSCD})^2 + (1 \cdot \delta\text{SCD}_{\text{ref}}^{\text{trop}})^2 + (\text{AMF}_{\text{ref}}^{\text{strat}} \cdot \text{VCD}_{\text{ref}}^{\text{model}} \cdot \delta s')^2 \\ & + (-\text{AMF}^{\text{strat}} \cdot \text{VCD}^{\text{model}} \cdot \delta s)^2]^{\frac{1}{2}} \end{aligned} \quad (3.14)$$

The uncertainty outputted by the fit is used for δdSCD , and an uncertainty of 10 % is assumed for $\text{SCD}_{\text{ref}}^{\text{trop}}$. The uncertainty of the respective scaling factors is determined via equation 3.15, where $\delta\text{VCD}_{\text{sat}}$ represents the precision of the stratospheric vertical column. All other quantities are considered to be precise, due to missing information on their uncertainty.

$$\delta s = \sqrt{\left(\frac{1}{\text{VCD}^{\text{model}}} \cdot \delta\text{VCD}^{\text{sat}}\right)^2} \quad (3.15)$$

To obtain the uncertainty of the VCD the uncertainty for the slant column is divided by the tropospheric AMF.

$$\delta\text{VCD} = \frac{\delta\text{SCD}^{\text{trop}}}{\text{AMF}^{\text{trop}}} \quad (3.16)$$

This value is then used for the uncertainty propagation of the NO_2 flux for every measured round, which is indicated by error bars in Figure 4.6 and Figure 4.7.

$$\delta F_{\text{NO}_2} = \sqrt{\sum_i (\delta \text{VCD}_i \cdot \vec{v} \cdot \vec{n}_i(s) \cdot \Delta s_i)^2} \quad (3.17)$$

Comparing between rounds, the fluctuations of the NO_2 flux are high compared to the calculated uncertainties. To capture the strong fluctuations the standard deviation from the mean flux is used instead to determine the standard deviation of the NO_x emissions (F_{NO_x}).

3.5 WRF-Chem settings and input data

The first model applied in this thesis is the Weather Research and Forecasting Model (WRF). It is a state-of-the-art model used for research and numerical weather prediction (NWP), maintained by an open-source community and originally developed in the latter 1990s. [89]

During that time, the widespread model used was the Mesoscale Model (MM5) [38]. However, it was nonconservative, used numerical approximations of low order, and did not feature portability, parallelism, extensibility or software layers. This marked the starting point of a successor, a shared NWP model for the research and operational groups, WRF. Its initial release was in the year 2000. [75]

The advanced research WRF, ARW, allows the configuration of WRF systems. It features several dynamic cores, choices for physical parameterization, is non-hydrostatic, and its options are customizable from large-eddy to global scale. The respective equations are solved in the Eulerian frame of reference. ARW is applied in various situations, e.g., real-time NWP, weather events, data assimilation development, atmospheric process studies, regional climate simulations and air quality modeling. [89]

The latter is of special interest in this thesis. Air quality modeling often makes use of WRF-Chem, here, version 4.2.2. It is a chemistry model fully coupled to WRF. The chemical equations are solved online, so in parallel to the meteorological equations [39]. The general process of running the model is similar to running only WRF, however, additional input data, as well as additional preprocessors, are required.

Initialization of the simulation is done with Reanalysis v5 data ($\Delta x \approx 31$ km, 137 vertical levels, hourly output) from the European Centre for Medium-Range Weather Forecasts [30]. The area of interest consists of two one-way nested domains over

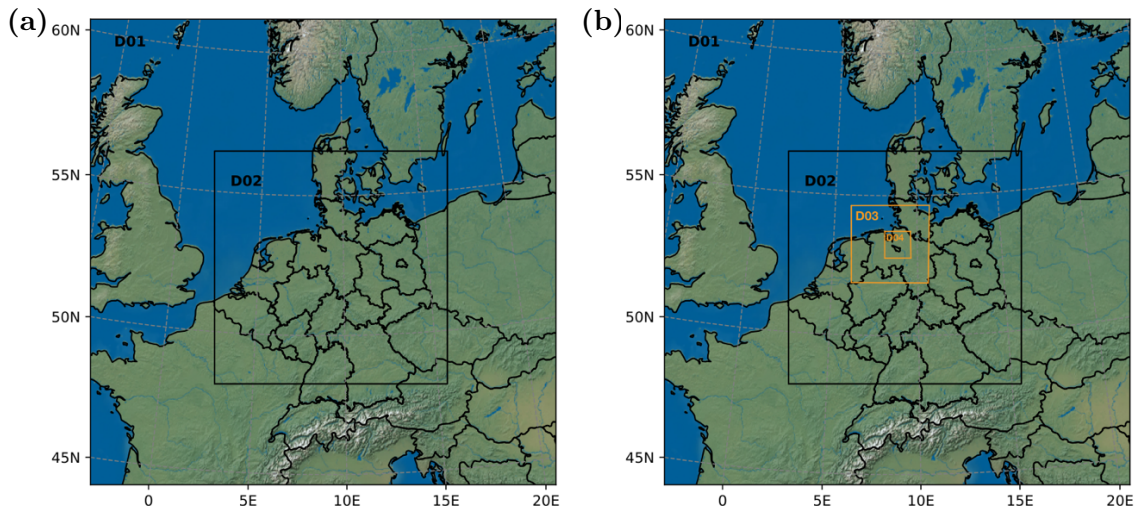


Figure 3.8: The simulated domains for the WRF-Chem runs. **a)** shows the domains used for the simulation of chemistry. Domain 1, centered at Bremen, includes large parts of Europe. It has a grid spacing of 30 x 30 km. The second domain focuses on northern Germany with a grid spacing of 10 x 10 km. **b)** Two additional domains are added for generating high-resolution meteorological output for FLEXPART-WRF. Domain 3 (3 x 3 km) primarily includes northern Germany, whereas Domain 4 (1 x 1 km) focuses only on the vicinity of Bremen.

northern Germany, where the horizontal grid spacing decreases from 30 km (61 x 61 grid points, $\Delta t = 180$ s) in Domain 1 to 10 km (91 x 91 grid points, $\Delta t = 36$ s) in Domain 2 (Figure 3.8a). The simulation extends from the 15th of June to the 1st of July, out of which the first 15 days account for the spin-up time of the model. Model output is generated every hour, and spectral nudging [62] is only applied on the outer domain. A full physical parametrization suite was used in the simulations (see Table 3.2 for details).

In addition, several WRF simulations were carried out using the same physical parametrization but without chemistry to be used as input data for the FLEXPART-WRF model. Two additional domains (centered over Bremen with 3 x 3 km and 1 x 1 km) are simulated to receive a higher spatial and temporal resolution of the meteorological variables around Bremen (Figure 3.8b). As a contribution to that, the output frequency is changed too, from hourly output to output every 30 minutes.

As a chemical mechanism, *mozart-mozaic-aq*, featuring MOZART Chemistry coupled with the MOSAIC sectional aerosol scheme, and aqueous phase chemistry is used [68, 72]. 85 gas-phase species, 12 bulk aerosol compounds, 39 photolysis, and 157 gas-phase reactions are implemented in MOZART-4. All reactions, rates, reaction probabilities, and further detailed information are found in the publication of Emmons et al. [32].

Auxiliary datasets are included to accurately reflect chemical emissions to achieve

Table 3.2: Model options used, common in all simulations except the photolysis option, which is only used with chemistry. The configuration files can be found in the appendix.

Atmospheric process	Scheme
Cloud microphysics	Morrison double moment [64]
Planetary boundary layer	Yonsei University PBL [45]
Cumulus parametrization	Grell 3D [36, 37]
Shortwave radiation	Dudhia Shortwave [25]
Longwave radiation	RRTM Longwave [63]
Surface layer physics	revised MM5 [50]
Land surface physics	Noah Land Surface Model [96]
(Photolysis)	Madronich photolysis (TUV) [59, 60, 67]

a realistic environment for chemical reactions. Briefly, some represent the anthropogenic, biogenic and biomass-burning emissions and others set the constraints for initial chemical concentrations as well as chemical boundary values. By utilizing preprocessors, provided by the Atmospheric Chemistry Observations and Modelling Lab (ACOM) of the US National Center for Atmospheric Research (NCAR), these datasets are translated into the WRF-Chem framework, which makes them readable during the simulation.

Emissions of prescribed burnings, wildfires and agricultural fires are featured by the finnv1 dataset [107]. The older version 1 is used because the latest version, finnv2.5, does not include the recent months. Fire_emis from the National Center for Atmospheric Research (NCAR) [66] is used to preprocess the data on burning biomass accordingly for WRF-Chem. Fluxes with a biogenic origin are represented by input data from MEGAN [40] from NCAR. This time Bio_emis from the NCAR [66] is used for preprocessing. Chemical input, as well as boundary data, is taken from the output of Whole Atmosphere Community Climate Model (WACCM) [61]. The preprocessor mozbc, downloaded from NCAR [66], initializes the respective values in the right format into the wrfbdy and wrfinput files. This is augmented by wesely and exo_coldens, which create additional files for the mechanism.

Anthropogenic emissions are represented by the CAMS-Glob-ANTv5.3 [35], distributed by ECCAD [21]. This inventory provides monthly emission values with a horizontal grid of $0.1 \times 0.1^\circ$ including 36 species and 20 different sectors, e.g. ships, power generation and refineries [21]. As CAMS-Glob-AIR possesses a horizontal resolution of only $0.5 \times 0.5^\circ$ [21], these coarse emissions, regarding Aviation, are not included. The efforts to allocate the aircraft emissions properly by height outweigh the benefits for the regional analysis.

To account for the anthropogenic emissions' temporal variability, the monthly values of CAMS-Glob-ANTv5.3 are scaled with diurnal cycles to represent sector-specific

hourly values using the High-Elective Resolution Modelling Emission System version 3 (Hermesv3_gr). It is a preprocessor developed by the Earth Sciences Department of the Barcelona Supercomputing Center and distributed as open-source [41]. The diurnal cycles, taken from Crippa et al. [18], are applied individually for every sector. Instructions on how to use Hermesv3_gr with WRF-Chem are located in the appendix. A weekly cycle is not implemented.

3.6 Evaluation of WRF-Chem output

The model output of WRF-Chem is evaluated with the help of observations. Three different types of datasets, surface meteorological stations from the Deutscher Wetterdienst (DWD), atmospheric soundings from University of Wyoming and surface air quality stations from Umweltbundesamt, are present. In this work, only stations around the area of interest are used to evaluate our model state. All the considered stations around Bremen are depicted in Figure 3.9.

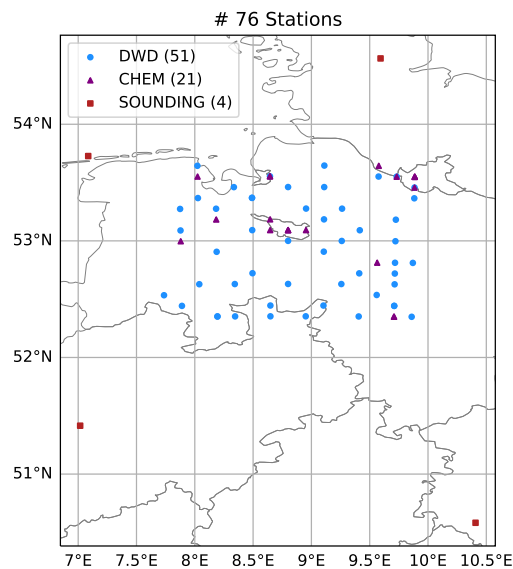


Figure 3.9: The locations of the measurement stations used for comparison. The four stations used for atmospheric profiles, red squares, consist of the closest sounding stations to Bremen and surround the city from all directions. 21 air quality stations in close proximity to Bremen, indicated with a purple triangle, are evaluated. Furthermore, 51 meteorological stations, depicted by blue circles, of the DWD are considered in the comparison. All stations are sufficiently far away from the borders of the second domain.

The first dataset consists of observations conducted by a network of the DWD. More than 1000 meteorological stations collect data, including secondary stations [26]. The observational period ranges from historical data, eg. 1937 for some stations, to recent data with only one day delay. The dataset can be obtained freely via the Climate Data Center [27, 28, 29]. The considered stations around Bremen add up to 51 from the DWD.

Profiles of atmospheric soundings are the second type of observation used for the comparison. Every 12 hours, they are recorded with radiosondes and utilized to evaluate the simulated atmospheric state at specific altitudes [104]. Seven stations are located in Germany. However, only the closest four to Bremen (WMO code: 10035, 10113, 10410, 10548) are considered for the comparison.

The third dataset contains concentrations of certain species relevant to air quality. The stations are located all over Germany, and their data is openly available on the website of the Umweltbundesamt [99, 100]. Out of all stations, 21 air quality stations close to Bremen are considered for comparison. These stations are further subdivided, depending on their location, by the Umweltbundesamt into traffic, background, and industry.

A useful quantity for the comparison of a model with observations is the bias

$$BIAS = \frac{1}{N} \sum_i^N (x_i - \tilde{x}_i), \quad (3.18)$$

where x_i represents the values from observations and \tilde{x}_i the model output. The bias indicates whether there is a general under- or overestimation by the model. A positive value represents an underestimation.

Another quantity is the root-mean-square error (RMSE). It indicates the deviations between the model output and the actual observations.

$$RMSE = \sqrt{\frac{1}{N} \sum_i^N (x_i - \tilde{x}_i)^2}. \quad (3.19)$$

3.7 Plume modeling with FLEXPART-WRF

The second model used in this work is the FLEXible PARTicle dispersion model coupled with WRF v3.2.2 (FLEXPART-WRF). It is based on and originated from FLEXPART [92], which is managed as open source and was published for the first time in 1998. [12]

FLEXPART is a transport and dispersion model. It is capable of simulating long-range and mesoscale transport, diffusion, dry and wet deposition and the radioactive decay of tracers. In contrast to WRF, it uses the Lagrangian frame of reference and is, therefore, independent of the computational grid. [93]

Further features of FLEXPART are the specification of the emission surface (point, line, area, volume) and the possibility of changing the modeling direction. Modeling

forward in time enables the analysis of dispersion. Modeling backward in time can be used to determine potential source contributions. More technical details on FLEXPART can be found in the manual from v8.2; see Stohl et al. [93].

In this study, the plume of the waste incineration plant is estimated by a forward simulation on the days when DOAS measurements were carried out. Two different approaches are used, described in the following.

Firstly, output with a lower resolution (10 x 10 km) is generated. It is used for comparison with the WRF-Chem output to estimate the impact of the waste incineration plant in the region. Secondly, a high-resolution output domain is simulated to follow the plume more closely. The runs only differ in the resolution of the input meteorological parameters and the output grid. For the coarser output, the meteorological variables from domain 2 (10 x 10 km) are used. For the fine grid, the meteorological variables from domain 4 of the auxiliary WRF run are used.

The mol weight of NO_2 , 46 g mol^{-1} , and a decay time (\tilde{t}) of 4.15 h is used, which represents a lifetime (τ) of 6 h. The conversion is done via:

$$\tilde{t} = \ln(2) \cdot \tau. \quad (3.20)$$

All other options for the species, e.g. wet scavenging or reactions with OH, are turned off for simplicity and are indirectly included via the lifetime. A lifetime of 6 h in summer is reasonable, as discussed earlier in section 3.4.

The waste incineration plant in Bremen is implemented as a point source at the respective location. The chimney stack has a height of 75 m, which is used as the emission height (This piece of information was obtained via personal communication with the operator, swb). The total release of NO_x (assuming a weight of NO_2) equals 1071.23 kg per day, which was calculated by assuming constant emissions over the year from the published annual value of 2020 of 391 000 kg [76].

FLEXPART-WRF uses an altitude-based grid for the vertical levels. To have a comparable grid with the WRF-Chem run, the average height of the respective vertical level of the WRF-Chem grid is computed and used. The height calculation is carried out for the 1 x 1 km domain over Bremen for both approaches. The input file for the high-resolution run of one date is found in the appendix.

Chapter 4

Results

In this chapter, the results are presented. Starting with the experimental side, maps with NO_2 concentrations and the emission calculation are shown, followed by the comparison of the model run with local stations and finishing with generated plots of the plume, which are then used to assess the importance of the waste plant as a local emitter.

4.1 DOAS measurements results

4.1.1 Meteorological situation

Bremen, located in northern Germany, is a city with a relatively mild climate. The weather data for June 2022, measured by the DWD stations at Bremen airport [26], is shown in Figure 4.1. On the left-hand side, a wind rose shows the distribution of wind direction and speed for June 2022 at Bremen airport. It is visible that the primary wind directions are west (W) and southwest (SW), which are accompanied by wind speeds up to 9 m s^{-1} . Around 16% of the time, the wind comes from a northern or northeastern direction. On the right-hand side, an overview of daily quantities is shown: hours of sunshine, precipitation, mean temperatures and cloudiness at Bremen. June this year was a dry and sunny month. Only specific days had a totally clear sky; most of the time, a cloudy sky was present.

Weather conditions play a role for different reasons: For DOAS measurements, clear-sky conditions or a homogeneous complete cloud cover is favorable to minimize the influence of varying light paths. Furthermore, with the setup used not being waterproof, rain conditions prohibit taking measurements. For investigating emissions, the wind should preferably originate from a low background region, which depends on the location of the respective source. Additionally, a constant and significant

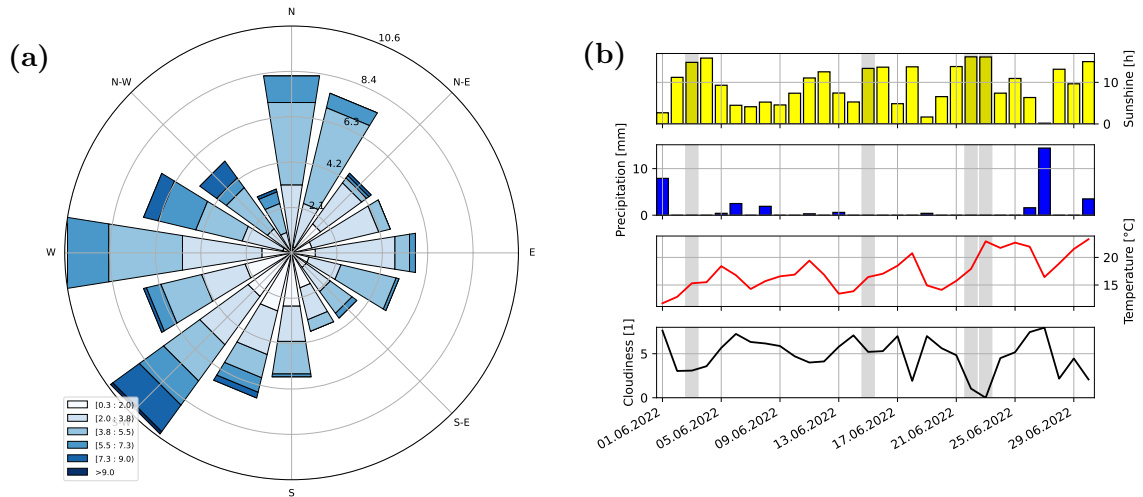


Figure 4.1: A meteorological overview for June 2022 at the Bremen airport weather station. **a)** shows a wind rose, indicating the distribution of wind direction and speed. **b)** shows the daily hours of sunshine, daily precipitation, daily mean temperature and daily mean cloud coverage. The values of cloudiness range from 0, representing a clear sky, to 8, referring to a completely covered sky. The measurement days in June are indicated by gray shading.

wind speed should prevail for optimal results. Having all those constraints in mind next to the weather forecast, measurements were taken on the 3rd, 15th, 22th, and 23rd of June 2022. Little cloud coverage was present during some measurements, but the sky was clear most of the time.

4.1.2 Bicycle DOAS results - waste incineration plant

Figure 4.2 shows the NO_2 vertical column around the waste incineration plant. The black dot represents the location of the chimney of the facility. In the top right, the wind direction and speed for that hour are shown. The wind is blowing from the northeastern direction to the southeast, hence from a rural area to the city. Colored dots indicate the vertical columns of NO_2 . It is visible that in the inflow region, the vertical columns are low compared to the outflow side. The maximum signal can be found downwind of the chimney.

Figure 4.3 shows maps of all rounds except for round 11, which is already shown above. Missing data points at a certain region, e.g., round 1, result from an unstable connection with the measurement computer or from the postprocessing by projecting the actual route to the ideal route, as explained in section 3.4. Rounds one and two were taken in February and March and had an elevated signal compared to measurements in June. Generally, most rounds show a higher signal in the outflow area. As described earlier in section 3.4, rounds 1, 12, and 16 do not match the

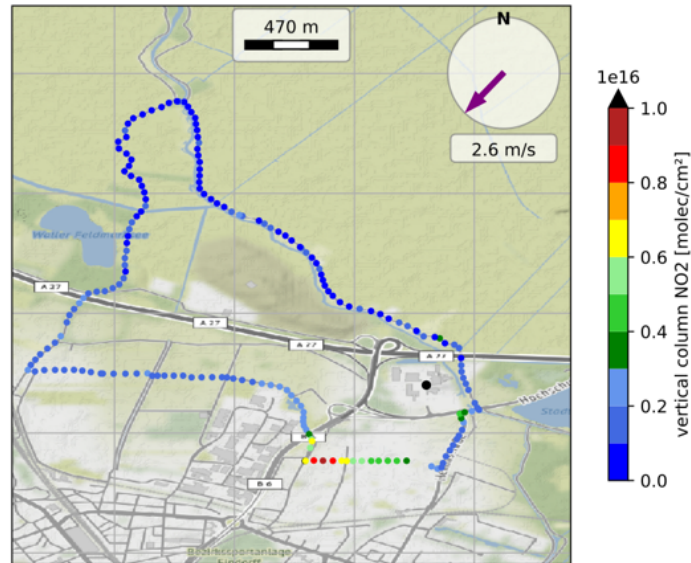


Figure 4.2: Map showing the measured NO₂ VCD from 15th June 2022 in round 11 around the waste incineration plant in northern Bremen. The black dot indicates the location of the chimney. The wind direction and speed from the DWD [29] are found in the top right.

defined criteria and are therefore excluded from further analysis.

The seasonal variations of the NO₂ VCD for the waste incineration plant and airport can be explained via the different lifetimes for NO_x in winter and summer. Whereas in summer, the lifetime of NO_x averages multiple hours, in winter, it can go up 21 h [87]. This is a consequence of lower concentrations of OH, as the hydroxyl radical is involved in the main loss process for NO_x, reaction 2.4. The production of OH depends on photolysis, which results in lower concentrations in winter [87]. Next to the higher lifetime, the power usage is higher in winter [81], which would result in higher emissions.

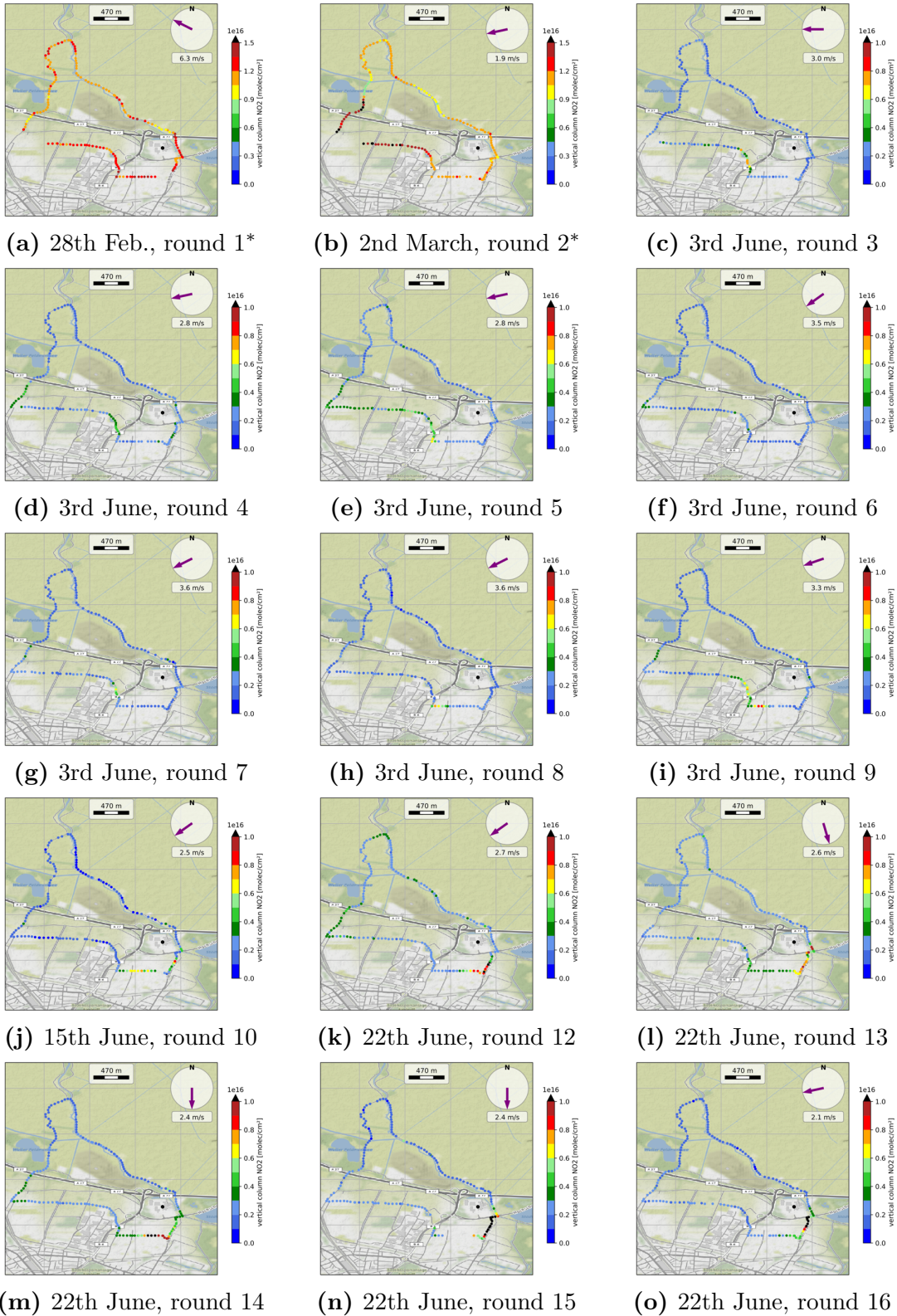


Figure 4.3: Maps of all measurement rounds (except 11, see figure 4.2) around the waste incineration plant. Colored points indicate the vertical column of NO_2 at the location of the measurement. Missing data points are a consequence of either a loose connection of the Avantes to the computer or the consequence of the projection to the ideal route, see section 3.4. The upper limit of the color bar is modified for figures labeled with *. The elevated signal at the start of the year is due to higher lifetimes of NO_x in the troposphere.

4.1.3 Bicycle DOAS results - airport

Two examples of the measurements around the airport are presented in Fig. 4.4. On the left, round three, measured on the 18th of May with one Avantes, is shown. In general, the vertical columns of NO_2 are more homogeneous, and the values do not exceed $0.6 \times 10^{16} \text{ molec cm}^{-2}$. On the right-hand side, round five, measured on the 23rd of June, is shown. This was taken with two Avantes on an adapted route. Having two Avantes enabled skipping measurements, where the driving direction is parallel to the wind direction, which leads to the gaps in the plotted round on the south and north. One Avantes was utilized upwind and one downwind of the airport.

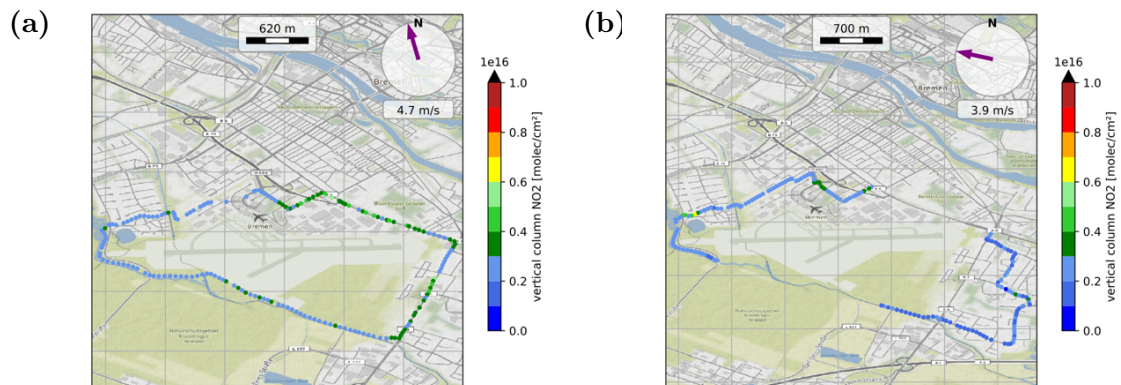


Figure 4.4: Maps of the NO_2 VCD measured in round 3 (left) and round 5 (right) around the airport of Bremen. **a)** shows the route when measuring with one Avantes. **b)** shows the adapted route with one Avantes deployed at the inflow region (east) and the other at the outflow region (west). The wind direction, as well as wind speed, is again depicted in the top right.

Figure 4.5 shows the maps of every measurement around the airport. Starting from round 4, two Avantes are applied for the measurements. Gaps in the measurements in the influx region originate from an unstable USB connection between the computer and the Avantes. The rounds taken earlier this year show an overall elevated signal, similar to the waste incineration plant. Round 1 and round 2 have their maximum signal in the inflow region, whereas the other rounds are more homogeneous and have some elevated values at the outflow area.

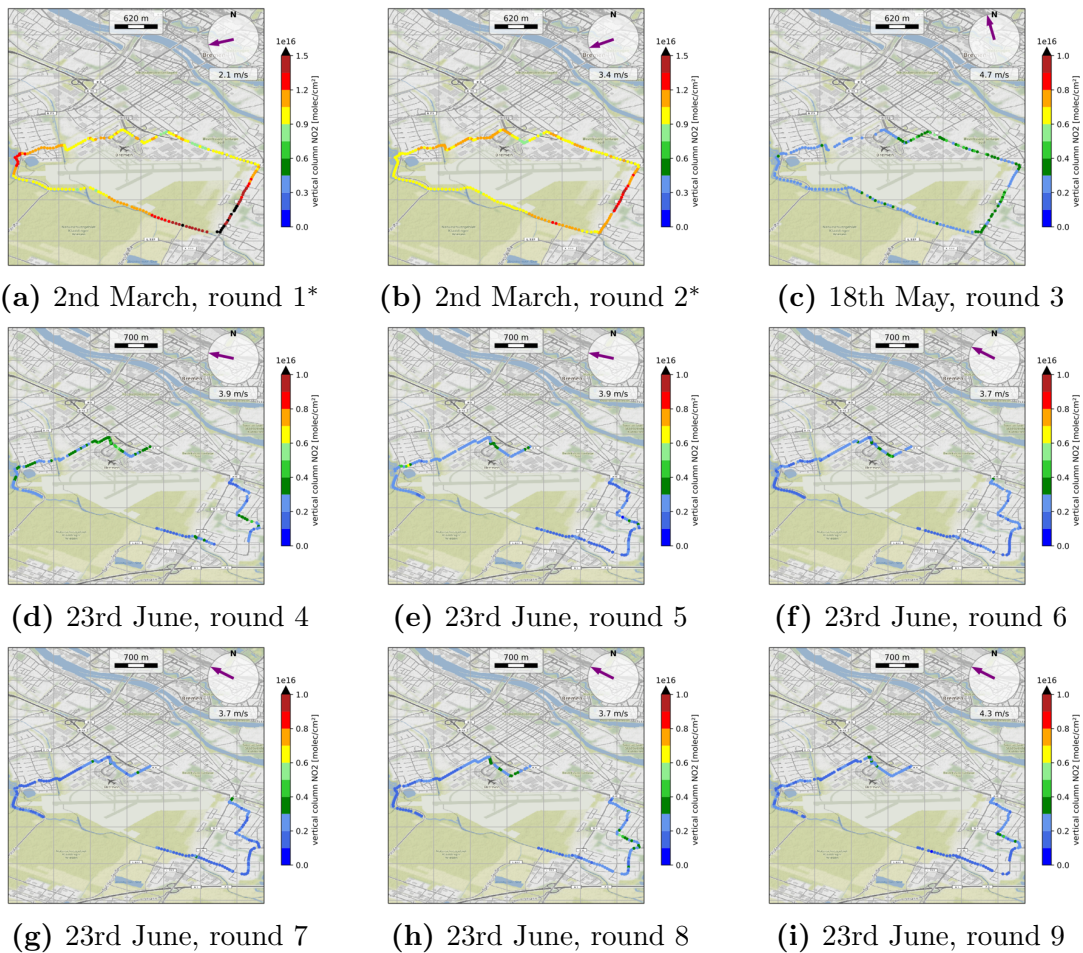


Figure 4.5: Maps of all measurement rounds around the airport. Starting with round 4, two Avantes were used, enabling skipping measurements where the driving direction is aligned with the wind direction. The other missing points, e.g., round 4, are a consequence of connection issues between the computer and the Avantes. Colored points indicate the vertical column of NO_2 at the location of the measurement. The upper limit of the color bar is modified for figures labeled with *. The elevated signal at the start of the year is due to higher lifetimes of NO_x in the troposphere.

4.2 Comparison of calculated emissions

The emissions calculated for the waste incineration facility are shown in Figure 4.6. The flux of NO_2 is depicted using a box plot for all the rounds (labeled on the x-axis). In total 16 rounds, each $\approx 10\text{ km}$ long, were carried out, out of which 13 are evaluated. For further details, check section 3.4. The error bars show the uncertainties due to the DOAS fit and postprocessing, section 3.4.1. The symbol on the bar indicates the respective measurement day for every round. All the dates shown are weekdays. Removing rounds 1, 12 and 16 from the analysis, the remaining rounds result in a positive emission signal. Averaging over the emissions yields $(8.7 \pm 2.8) \times 10^{22} \text{ molec s}^{-1}$ of NO_2 . Converting that flux to NO_x with the help of equation 3.12 returns annual NO_x emissions of $(291 \pm 95) \times 10^3 \text{ kg a}^{-1}$.

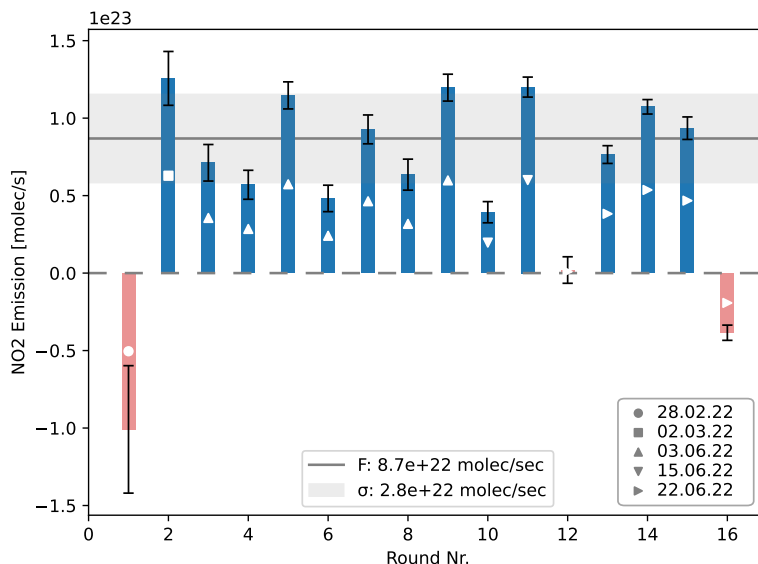


Figure 4.6: Emissions from the waste incineration facility for every round. Rounds 1, 12 and 16 (red) are not evaluated, see section 3.4. The error bars indicate the uncertainties due to the DOAS fit and postprocessing. The symbol on the bar refers to the date of the measurement. The gray line represents the mean value (excluding the red values), and the gray-shaded region indicates one standard deviation.

The emissions of the airport are depicted in Figure 4.7. All rounds were taken on weekdays. The symbol on the bar indicates the respective date. The gray line indicates the mean value of $(2.2 \pm 4.7) \times 10^{22} \text{ molec s}^{-1}$, and the gray shaded area depicts one standard deviation. The standard deviation is larger than the calculated mean, which originates from a larger variation, especially visible in the first rounds. The error bars illustrate the uncertainties attributed to the DOAS Fit and the postprocessing. Calculating the emission fluxes for the airport yields $(52 \pm 113) \times 10^3 \text{ kg a}^{-1}$ for NO_2 and $(72 \pm 155) \text{ kg a}^{-1}$ after the conversion to NO_x .

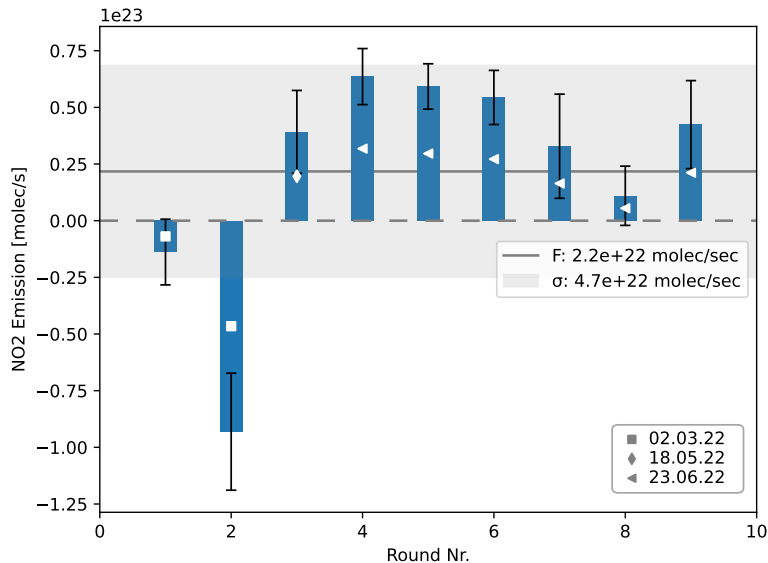


Figure 4.7: Emissions from the airport of Bremen for every round. The error bars indicate the uncertainties due to the DOAS fit and postprocessing. The symbol on the bar refers to the date of the measurement. The gray line represents the mean value, and the gray-shaded region indicates one standard deviation.

4.3 Comparison of WRF-Chem output with observations

Compared to meteorological variables from the surface stations, model surface temperature correlates with observations, see Figure 4.8a. Only little deviations are present, indicated by a low bias and low RMSE.

For the model wind speed, Figure 4.8d, it is visible that more points lie above the 45° line, which indicates a bias of the model towards overestimation. For surface humidity, Figure 4.8b, the outcome looks similar.

The hourly precipitation, Figure 4.8e, is an example of a poor correlation, even though the bias and RMSE are relatively small. The correlation improves when comparing daily precipitation, Figure 4.8f by summing up all 24 hours. Overall rainfall is overestimated by the model, mirroring the overestimation in relative humidity.

The surface wind direction, depicted in 4.8c, shows good agreement between the model output and the station. Due to its periodicity, the scattered points around (0,360) and (360,0) are still close to the ideal agreement. The worst-case scenario would be a deviation of 180°, represented by the additional dashed lines.

In general, the near-surface weather characteristics are represented within the expectations of a mesoscale model [43]. It fails to capture the hourly precipitation, but over the day, it correlates well with the observations.

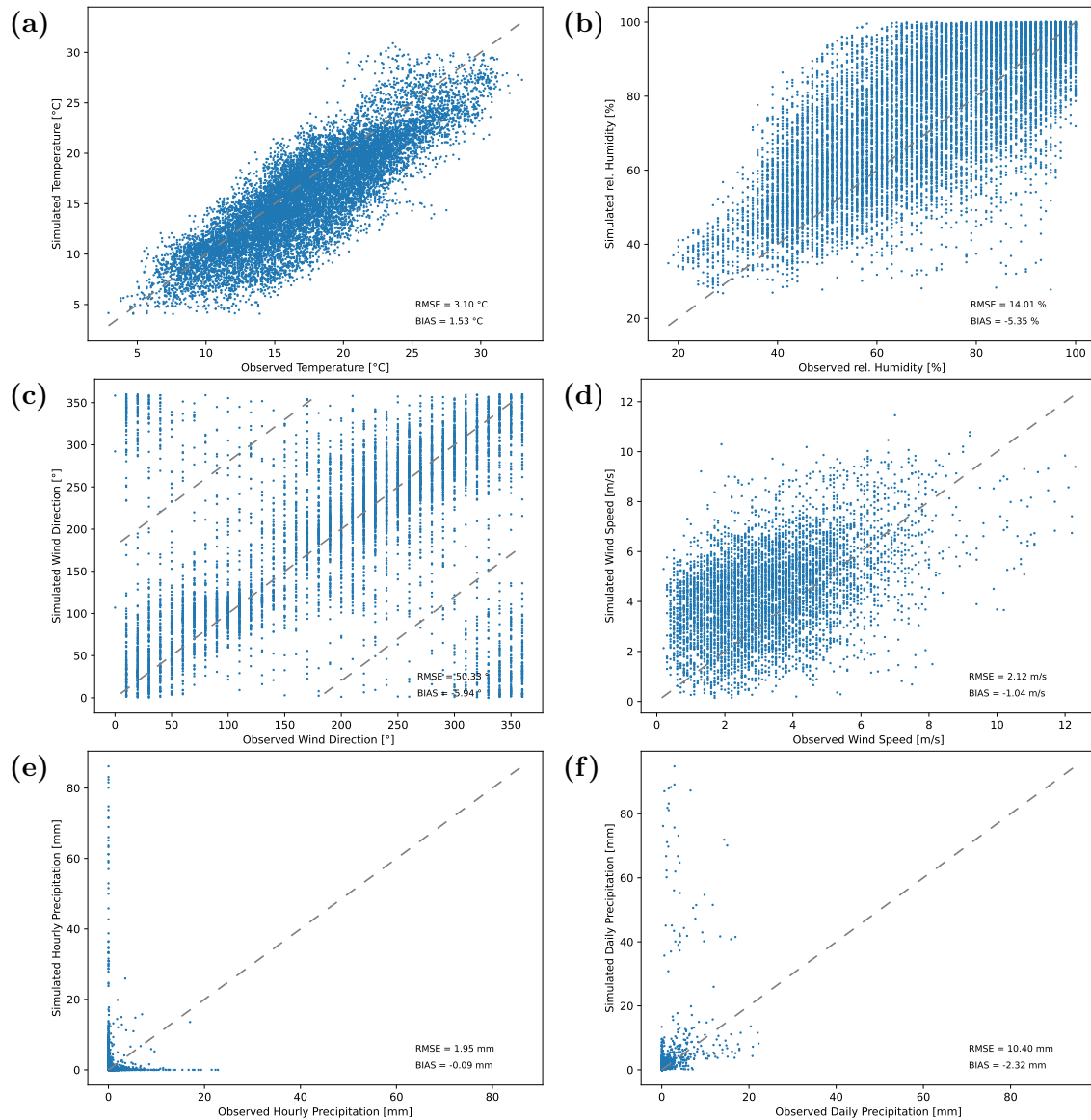


Figure 4.8: Overview of meteorological parameters of domain 2 of the WRF-Chem simulation compared against observations from surface stations over the simulation period (excluding spin-up of 2 weeks). For each subfigure, the modeling quantity is plotted against the observation. An ideal correlation would be represented by only points on the line angled at 45° . Furthermore, RMSE and bias of the model for that quantity are given in the bottom right, where a positive bias would indicate an underestimation by the model. **a)** shows the temperature, **b)** relative humidity, **c)** wind direction, **d)** wind speed, **e)** hourly precipitation and **f)** depicts daily precipitation.

The second important comparison is conducted to evaluate how the simulated meteorological characteristics behave with altitude. An example sounding is depicted in Figure 4.9. Here the pressure is plotted against the temperature, which illustrates how the temperature changes with altitude. It is visible that the model follows the observations quite closely but fails to capture quick temperature changes.

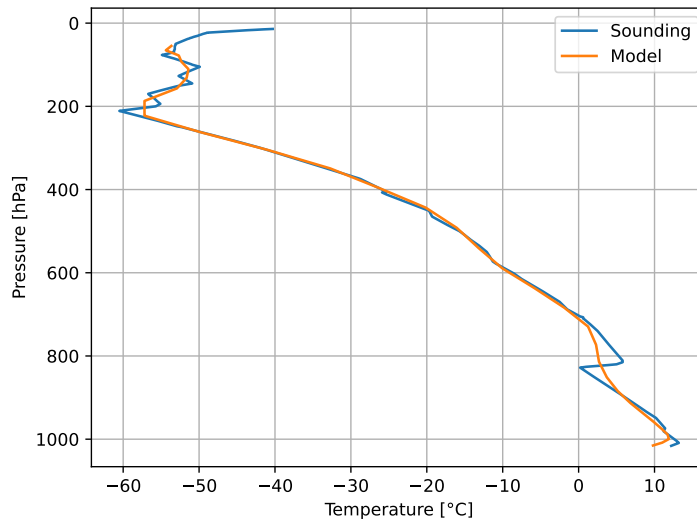


Figure 4.9: Temperature sounding on 15.06.2022 for the sounding station located in the north (Schleswig Holstein). It shows how the temperature changes with altitude in observations and how well the model captures those.

Model simulated data are interpolated to certain altitudes for comparison with observations and then the RMSE and bias are calculated after averaging all atmospheric soundings and all stations (Figure 4.10). Here the bias and RMSE for the meteorological variable are depicted against the pressure, hence the altitude.

RMSE reaches a maximum in the free troposphere for all quantities except wind direction, whereas the bias stays relatively constant over the whole atmospheric profile. As the pollutants are released at the surface, the bias and RMSE are noted for the planetary boundary layer, shaded in gray. The last pressure level included is 850 hPa. The performance of the model above the PBL is not the focus here.

As seen with the evaluation against the surface stations, the model results compare well against the observations, especially when focussing on the planetary boundary layer. Mirroring the surface station results, the relative humidity is overestimated across the atmospheric profile. Finally, wind direction shows an increased error compared to the surface observations; however, it should be noted that the comparison is carried out using four stations and is, therefore, more susceptible to single data points.

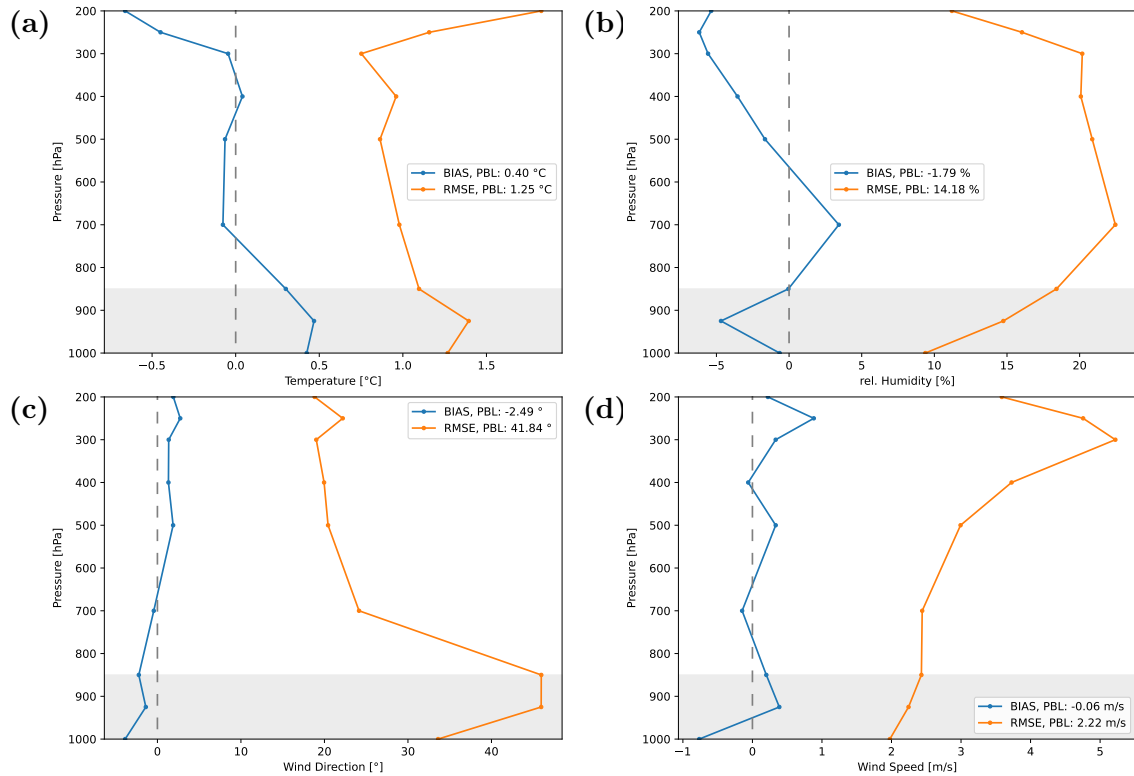


Figure 4.10: Comparison of simulated meteorological variables of domain 2 with observations for different pressures, hence altitudes. Here the bias and RMSE are averaged over all soundings of all stations, where a positive bias would indicate an underestimation by the model. **a)** shows the temperature, **b)** relative humidity, **c)** wind direction and **d)** depicts the wind speed.

Now the near-surface chemistry is compared with observations. The pollutants CO, NO₂ and O₃ are shown in Figure 4.11. On the left, the averaged diurnal cycle of all measurements is depicted. On the right-hand side, the model output is plotted against the station values.

Starting with CO: The diurnal cycle, Figure 4.11a, is too small by a factor of two, and it does not follow the same variability. Furthermore, the simulated concentration of CO never subsides a certain threshold, see Figure 4.11b. The stations assigned to the traffic category are underestimated the strongest.

Modeled NO₂ concentrations (Fig. 4.11 c,d) show a realistic diurnal cycle. Still, the model underestimates the concentration by at least a factor of 3. This underestimation can be found again in the scatter plot, where most data points are below the 45° line, especially the traffic data points.

O₃ has the best agreement between the model and the observations. Similar curve progression and similar magnitude are visible in Figure 4.11e. A slight overestimation during the morning hours and a slight underestimation after noon are visible, which results in similar average values for the concentrations from the simulation

and observations. The scatter plot, Figure 4.11f, indicates some overestimation happening for the model output.

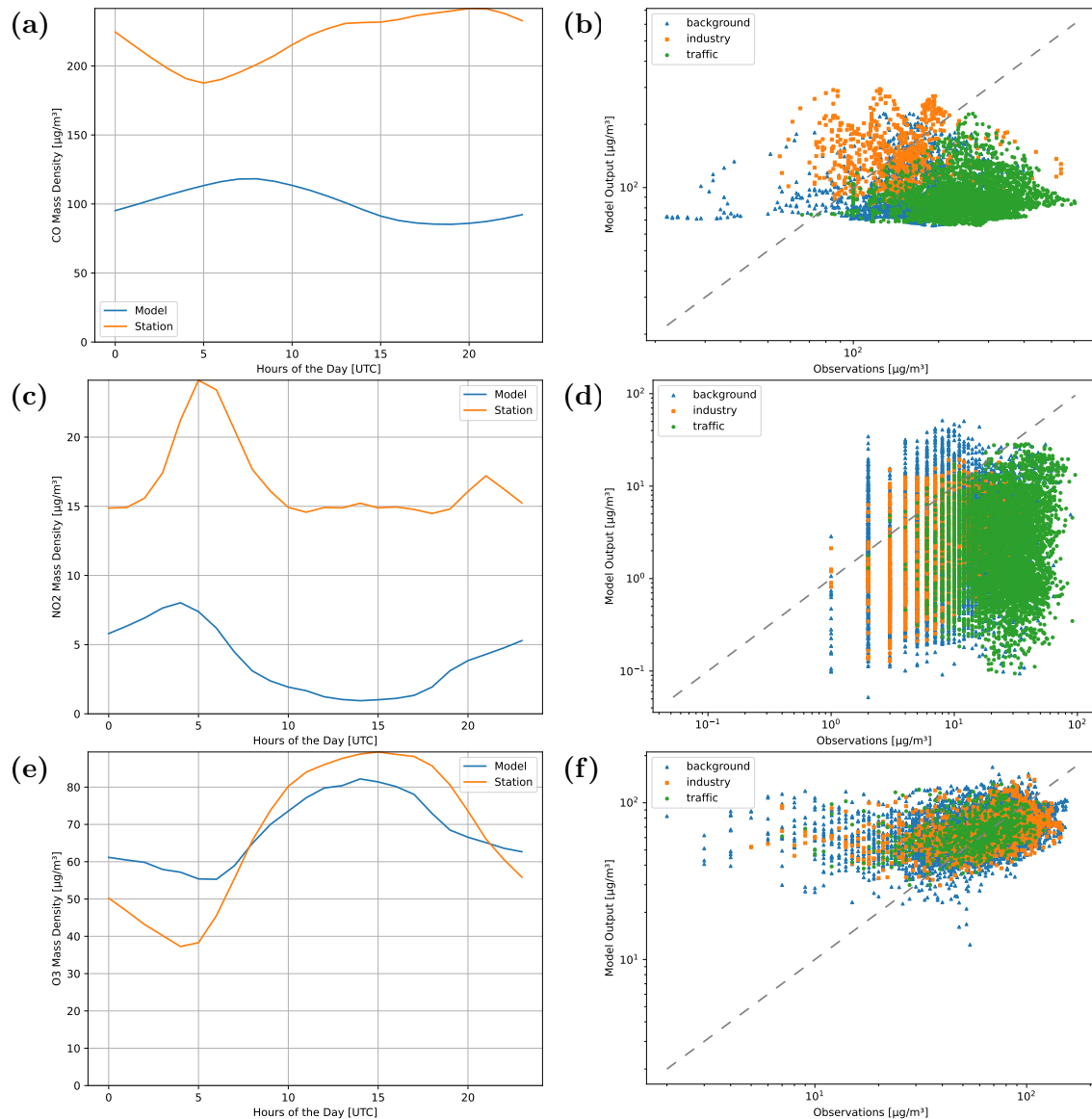


Figure 4.11: Overview of chemical species of domain 2 of the WRF-Chem simulation compared with observations. On the left, the average diurnal cycle for the respective pollutant is depicted. On the right, the model output is plotted against the station values on logarithmic axes. The different categories of air quality stations are colored accordingly. a) & b) represent CO, c) & d) NO₂ and e) & f) depict O₃.

To conclude, the model is able to depict the meteorological parameters on the surface with good precision, as well as the ozone. Moreover, the accuracy of the soundings is good. However, the simulation of humidity and precipitation can be improved together with the precision of predicting atmospheric profiles. Furthermore, the model fails to capture the diurnal cycles of the precursors of O₃.

4.4 Assessing importance of the waste incineration plant as an emitter

Special focus is directed on the days when DOAS measurements were taken by bicycle in June. The evolution of the NO_x plume, generated by FLEXPART-WRF, on 15.06.2022 is shown as an example below. The red dot indicates the location of the waste incineration plant in Bremen.

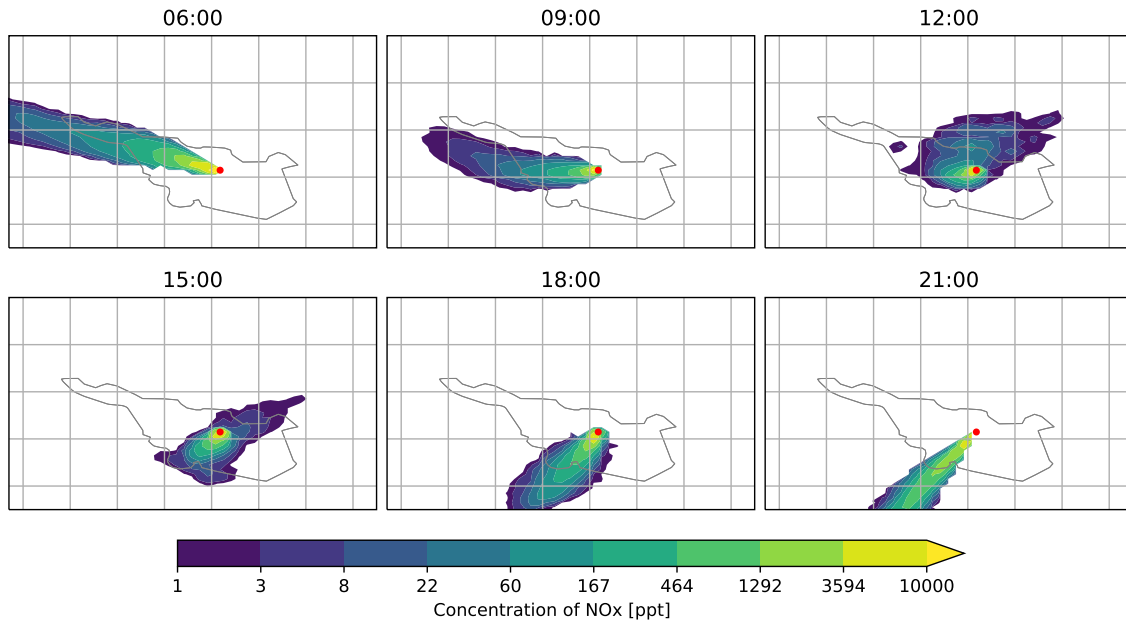


Figure 4.12: Simulated time evolution of the NO_x plume from 15.06.2022 for the waste incineration plant. The red dot indicates the facility's location and the gray outline refers to the boundaries of Bremen. The concentration of NO_x is colored with a logarithmic spacing. The time is given in UTC.

After the spinup of 6 h, the plume stabilized towards the west. In the next hours, the wind speed decreases, and the plume of NO_x remains close to the waste incineration plant. Towards the afternoon, the wind speed increases again, this time pointing towards the southwest, which results in the plume extending further than the outlines of Bremen. The concentrations exceed 10 000 ppt (10 ppb) in the center around the source.

These simulations are run for every measurement day in June on a coarser output grid. The coarsely gridded concentrations of FLEXPART are used to determine the NO_x fraction of the total concentration (f) originating from the waste facility for every point on the grid, in the following called NO_x fraction.

$$f = \frac{\tilde{C}_{\text{NO}_x}}{C_{\text{NO}_2} + C_{\text{NO}}} \quad (4.1)$$

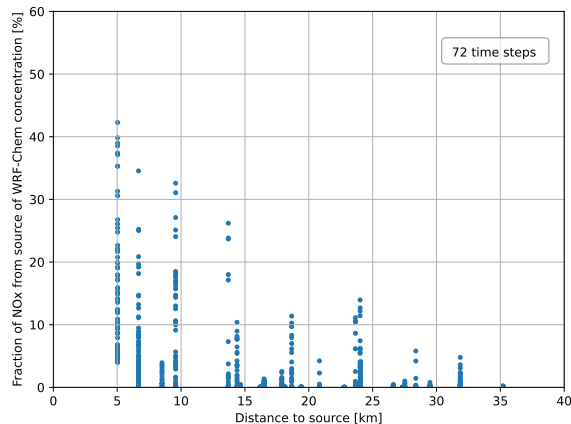


Figure 4.13: The distribution of the NO_x fraction of the total concentration originating from the waste facility is visualized. The fractions at every grid point are plotted against the distance to the facility. 72 timesteps (excluding spin-up) are shown.

Here \tilde{C}_{NO_x} denotes the concentration from FLEXPART, whereas the concentrations from WRF-Chem are represented without a tilde. To capture potential vertical mixing, the sum of the first eight layers is analyzed, which on average, equals an altitude of 1 km.

The first figure to discuss is Figure 4.13. The NO_x fraction is plotted against the distance. It is visible that the high fractions occur close to the source and the abundance of high fractions decreases rapidly with the distance. Furthermore, the fractions are not evenly distributed over distance, especially below 10 km. The highest fraction at one timestep results in 42% of the NO_x concentration being attributed to the waste incineration plant.

To retrieve the spatial distribution of the influence of the waste incineration plant on air quality, Figure 4.14 gives some insight. The black dot indicates the location of the waste incineration facility. On the top left, the average background concentration of NO_x (over all 72 timesteps) generated by WRF-Chem is shown. To the right, the average concentration simulated by FLEXPART-WRF originating from the waste incineration plant is shown. Note the different color scalings. In general, the concentrations generated by FLEXPART-WRF are approximately one order of magnitude smaller.

Calculating the average NO_x fraction of the total concentration over all 72 simulated timesteps results in Figure 4.14c. The fraction is highest, between 14% and 16%, at the grid point where the waste incineration plant is located. The fraction exceeds the background value towards the west and southwest.

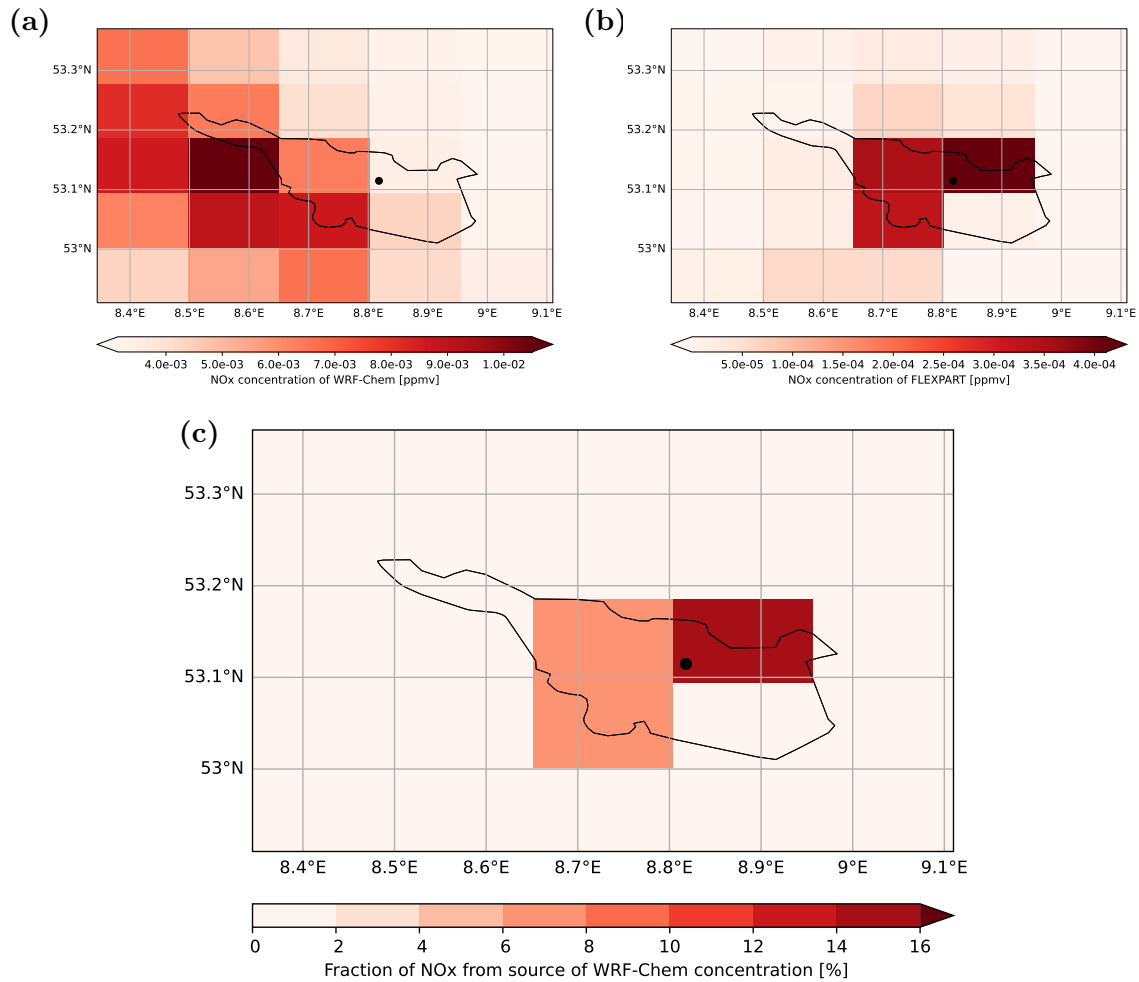


Figure 4.14: The gridded output NO_x concentrations for the different models, averaged over four days in June, are depicted. **a)** shows the averaged total NO_x concentration, simulated by WRF-Chem. **b)** depicts the average concentration, which can be attributed to the waste incineration plant generated by FLEXPART-WRF. **c)** shows the resulting fraction of NO_x concentration originating from the waste facility. It is obtained by dividing the concentrations of FLEXPART-WRF by the concentrations of WRF-Chem. The black dot refers to the location of the facility, and the outline of Bremen is shaded in black.

Chapter 5

Discussion

This chapter discusses the results from the previous chapter. It covers to what extent assumptions of the applied method are valid or accurate and contextualizes the ability of the model to reproduce observation. Lastly, the expressed pattern in the visualization of the impact of emissions by the waste incineration plant is explained.

5.1 Emission calculation

A comparison value for the waste incineration plant for validating the method is found in the Pollutant Release and Transfer Register (PRTR) [76]. The latest information states that $391 \times 10^3 \text{ kg a}^{-1}$ of NO_x were emitted in 2020. This number is located slightly outside of the interval $[196 \times 10^3 \text{ kg a}^{-1}, 386 \times 10^3 \text{ kg a}^{-1}]$ based on one standard deviation of the calculated mean. Hence the emissions of the waste incineration facility are underestimated by the applied method. This underestimation is reasonable, considering all the uncertainties related to the used method.

Furthermore, the value in this study is obtained primarily from June and extrapolated to yield an annual emission. The calculated values from 2022 had to be compared with the reported values for 2020. Both can introduce a deviation that is not yet accounted for.

The rather high variation of the emissions of the single rounds, represented by a large standard deviation of ($\sigma = 2.8 \times 10^{22} \text{ molec s}^{-1}$), originates from various reasons:

- a) No constant atmospheric conditions
- b) Varying concentrations in the inflow region
- c) Wind field not known accurately

- d) No cloud correction
- e) Different compositions of the fuel or waste mixture

The assumption that the atmospheric conditions stay the same is embedded in equation 3.11. If the wind field is not constant during one round, several effects can occur. The plume might not be straight, and a higher signal is retrieved when driving alongside the plume or the plume has not spread to the edge, where the measurements are taken, which results in underestimation.

Moreover, if the concentrations of pollutants in the air parcel vary strongly upwind of the measurement region, it might lead to a large variation in the calculated emission. It becomes important which air parcel is analyzed in the single measurement. For example, let's assume that a strongly polluted air parcel in the inflow region is analyzed and this specific air parcel is not present at the outflow region when the measurements are taken, due to various reasons (e.g. changing atmospheric conditions). Then the encircled area becomes a sink. This problem worsens with higher concentration differences in the inflow area and smaller emission sources, which become difficult to distinguish from the background.

Furthermore, an accurate wind field is required for calculations [49]. The hourly values provided are obtained from the airport, which is good for airport measurements but not ideal for the incineration plant, which is located 7 km further north. The measurements took approximately 40 minutes and were conducted consecutively. So for certain rounds, two different wind values are present, which could be avoided by averaging over a wind field with a higher temporal resolution for the measurement period to ensure that the assumption of a constant wind field is as accurate as possible. A simulated wind field, e.g. from WRF, could be used to improve accuracy.

No correction for clouds is implemented, even though the sky was, in general, not completely cloud-free. Lastly, the waste incineration plant produces power by burning waste. The emissions originating from waste combustion vary with changes in the composition [2]. It is likely, that the composition of waste changes during the day.

During the conversion from NO_2 to NO_x , see equation 3.12, a certain partitioning is assumed. This partitioning is highly dependent on the distance to the source because NO_x is mainly emitted as NO and gets converted to NO_2 in the plume to reach an equilibrium state [49]. Depending on what distance to the source the measurements are taken, a different fraction of NO_2 is present. By assuming one constant partitioning factor, significant uncertainty is introduced. [49]

The airport results differ drastically from the waste incineration plant, which can be expected due to the different emission characteristics, location and terrain. With the help of the definition of robust quality criteria, see section 3.4, certain rounds could be excluded from the calculation of emissions for the waste incineration plant. These quality criteria are difficult to check for the airport. Whereas the waste incineration plant possessed a clear plume on every measurement day, no clear plume is present for the airport. This impedes the selection of bad rounds because the wind direction can not be double-checked.

Furthermore, a negative emission signal can not be deemed unreasonable because the large area could enable deposition. Additionally, the emission signal might not be distinguishable from the background as the emissions are not constant and depend on the air traffic frequency. As a consequence of the Covid-19 pandemic, air traffic was significantly lower [11, 52]. During all measurements, only a few airplanes were visible. At most two airplanes were either arriving or departing during one measurement.

Multiple additional issues are present for the airport of Bremen. Firstly, it is nearly surrounded by the city, which results in many situations with a rather high signal at the inflow side. This increases the risk of obtaining negative emissions as a consequence of unstable atmospheric conditions or dilution to the background level.

To conclude, the DOAS method does not show a significant emission signal for the airport of Bremen with the limited data present due to a more difficult initial situation. In contrast, the method agrees well with the published emissions for the waste incineration plant when considering the various factors influencing the calculation of emissions.

5.2 WRF-Chem output

The WRF-Chem run simulates the near-surface weather characteristics well, and they do not deviate strongly from the observations. The large error in precipitation can be partially explained due to a misrepresentation in the timing of the rainfall, as correlation is improved for daily precipitation. Precipitation is a common drawback for NWP models, as multiple processes of different scales influence the formation of precipitation [19].

Generally, it has to be considered that the longer-needed spinup time for the chemistry interferes with meteorology. Meteorological variables need at least 12 h of spinup to reach equilibrium [8]. Going far beyond that point increases the chance of the meteorological variables deviating from observations, which is visible for wind

direction at certain altitudes.

The deviations in the diurnal cycle of the precursors of O_3 could originate from inaccurate input emissions. The accounted emissions of NO_2 and CO are too low compared with the observations. Moreover, the overestimation of precipitation by the model might be another origin for the deviation. Higher precipitation leads to higher wet deposition, decreasing the concentrations further. The diurnal cycle of ozone is captured well. This is surprising because ozone chemistry is strongly influenced by its precursors, which are heavily underestimated.

It has to be noted that the air quality stations are set side by side with coarsely gridded concentrations. Certain small-scale plumes, which the stations might measure like traffic, are not resolved in the model, naturally leading to deviations. The latter is visible in the missing prominence of the NO_2 peak during the morning and in the traffic data points in the scatter plots. For CO and NO_2 the data originating from stations classified as traffic stations (depicted in green) is strongly underestimated.

Comparing the representation of observations in the WRF-Chem simulation with the evaluation by Georgiou et al. [34] shows that the model output of this thesis exhibits similar properties. Georgiou et al. [34] show that their ozone levels are overestimated by approximately 20 %. In this study, the average concentration of O_3 over the day is comparable between stations and simulations. Furthermore, the simulation of Georgiou et al. [34] fails to capture the diurnal variations of NO_x and expresses an underestimation. Here, the averaged NO_2 concentration is underestimated too, but by forcing a diurnal cycle into the anthropogenic emissions the traffic peaks are captured in the diurnal cycle. It has to be noted that Cyprus has a complex topography in comparison to Bremen, which impedes the realistic representation of pollutants.

All in all, the model reproduces the observations sufficiently for this analysis, but especially the precursors of O_3 indicate that the model configuration could be improved.

5.3 Assessment on importance

Intuitively, the impact on air quality should decrease with distance, which is generally the case for Figure 4.13. Some data points stand out, which could be explained by varying concentrations in the WRF-Chem output for neighboring grid boxes. The discrete distribution of the NO_x fractions results from the gridding of the data. The waste incineration plant is close to the edge of its gridbox, which has a width of 10 km. This leads to the closest values being at a distance of approximately 5 km,

which belongs to the center of its box. In total, this figure follows the expectations.

The share of the total NO_x concentration originating from the waste incineration plant is the highest in close proximity to its location. This is reasonable because the emissions maintain a high concentration of NO_x over all timesteps. Furthermore, the higher values in the west and southwest can be explained by the wind directions during the four simulated days. This is consistent with the considerations regarding optimal conditions because wind directions from the north or northwest are favorable for analyzing the waste incineration plant as little background signal is present in the inflow area. This thought was a criterion for choosing the measuring days. If the plume would be simulated for the whole month, it should express a pattern closely related to the distribution of the wind direction for June, as depicted in Figure 4.1. Considering the underestimation of NO_2 by WRF-Chem, the fraction is potentially overestimated for the waste facility. Hence the calculated values are realistically upper bounds. The spatial distribution, however, should hold.

It should be noted, that concentrations near the ground level are especially relevant for health considerations, whereas, in this study, a layer up to 1 km altitude is analyzed. Furthermore, the emissions of the waste incineration plant originate at a height of 75 m, to minimize their near-surface impact.

To conclude, in proximity to the waste incineration plant, the upper limit of the NO_x fraction reaches 15 %. With increasing distances, the fraction drops significantly to the low percentage range, resulting in the waste incineration plant from swb being an important local emitter. However, its influence on air quality beyond Bremen is limited.

Chapter 6

Conclusion & Outlook

This thesis aimed to quantify the NO_x emissions and evaluate their impact on the air quality in Bremen for specific NO_x sources. To achieve this, bicycle DOAS measurements were conducted in 27 rounds around two emission sources. After correcting for diurnal cycles in the stratosphere, NO_2 emissions were derived following the divergence theorem of Gauss. The single-round emissions were averaged, converted to NO_x emissions and extrapolated to represent annual values. Afterward, a numerical weather prediction model coupled with chemistry was set up and run to simulate the atmosphere during June. Following the initialization of a flexible particle dispersion model with the meteorological variables, the NO_x plume of the waste incineration plant was simulated for the days of measurements. This spatial distribution of NO_x was then compared with the total concentration, generated by WRF-Chem, to assess the importance of the waste incineration plant as a local emitter for the air quality in Bremen.

The method of bicycle DOAS as a complementing mobile setup to the common platforms has certain advantages. It is possible to take smaller paths, enabling more flexible routing and a smaller distance to the source. Furthermore, the velocity is easily controllable, allowing adaptations of the spatial resolution during the ride. However, the smaller paths often do not provide a clear line of sight because the trees are not pruned (less profound problem in winter). Moreover, the extra weight of the measurement setup impedes taking many measurements, which is why an electric bicycle might be optimal for taking bicycle DOAS measurements.

The calculated emissions for the waste incineration plant show a good agreement with the reported annual emissions. Generally, the visible plume and the dominant wind direction from the low background area in the northeast facilitated the analysis of the waste incineration plant. In combination with the simulations, its local impact

on air quality was quantified, which refers to the fraction of NO_x originating from the facility compared to the total NO_x concentration around Bremen. At most 14-16 % of the NO_x originates from the waste incineration plant in the direct vicinity.

As expected, the weaker and intermittent emissions from the airport provided a more challenging target for the methodology. However, despite ultimately failing to lead to a statistically robust emission estimation, several important insights were obtained. Firstly, the importance of the location relative to the city was highlighted; due to the airport's position, it was difficult to isolate the emission signal from background city emissions. Additionally, a missing plume and suppressed emissions (low number of flights) from air traffic complicated the analysis.

Furthermore, the evaluation of the WRF-Chem output indicates that there is a discrepancy between the average concentration of ozone precursors measured at stations and the average simulated concentration. This hints at an underestimation of the emissions in the used datasets. It is likely that the anthropogenic emissions are underestimated, as the prominence of the NO_2 peaks is not fully replicated. A follow-up study conducting a sensitivity test could quantify the underestimation of the local emissions. Apart from that, the creation of a local data set for Bremen would enable the comparison with the CAMS-Glob-ANT to improve its accuracy.

Arranging long-term observations in succeeding studies for the airport would likely improve the performance of determining the emissions. After achieving a clear signal from the airport, the same procedure concerning the WRF-Chem and FLEXPART-WRF, could be used to estimate its local impact. Additionally, the availability of a high-resolution inventory for aviation-related emissions would extend the possibilities. Complementing the probing of surface-related emissions by DOAS, the sensitivity of the air quality in Bremen to aviation emissions allocated in higher altitudes by WRF-Chem would become possible.

Overall, combining the two augmenting approaches enables covering an emission source in more detail from multiple angles and serves as a good starting point for in-depth follow-up studies. Next to the long-term observations for the airport, sensitivity simulations with scaled emissions could follow to quantify which air quality restrictions would have the biggest benefit for Bremen, which could serve as a political road map.

Chapter 7

Acknowledgements

I acknowledge the use of the WRF-Chem preprocessor tool `mozbc`, `fire_emiss`, `bio_emiss`, `exocoldens` and `season_wesely` provided by the Atmospheric Chemistry Observations and Modeling Lab (ACOM) of NCAR.

Furthermore, thanks to Gara Villalba Mendez for helping me with the setup of `Hermesv3_gr` with WRF-Chem by providing their configuration files of the paper “A take-home message from COVID-19 on urban air pollution reduction through mobility limitations and teleworking” [4].

The contribution from Barbara Scherllin-Pirscher, by providing the updated version of the preprocessor of CAMS-Glob-ANTv5.3 for `Hermesv3_gr`, is greatly appreciated as it enabled using the newest version of the anthropogenic emission dataset.

All simulations were performed at the Aether HPC cluster at the University of Bremen, Laboratory for Modeling and Observation of the Earth System, supported by Marius Dan.

Thanks to Alex Poulidis and Kezia Lange for their quick help with all the encountered struggles, and for proofreading my thesis.

Lastly, special thanks to Mihalis Vrekoussis, Andreas Richter, the LAMOS, and the DOAS group for their great support, guidance, and feedback during the whole thesis.

Bibliography

- [1] Armerding, W., Herbert, A., Spiekermann, M., Walter, J., and Comes, F. J. “Fast scanning laser DOAS - A very promising technique for monitoring OH and other tropospheric trace gases”. *Fresenius’ Journal of Analytical Chemistry* 340 (1991), pp. 654–660.
- [2] Astrup, T., Møller, J., and Fruergaard, T. “Incineration and co-combustion of waste: accounting of greenhouse gases and global warming contributions”. *Waste Management & Research: The Journal for a Sustainable Circular Economy* 27.8 (2009), pp. 789–799. DOI: 10.1177/0734242x09343774.
- [3] AVANTES. “Optical Spectrometers: an introduction”. (2022). URL: <https://www.avantes.com/support/theoretical-background/introduction-to-spectrometers/> (visited on 4.10.2022).
- [4] Badia, A., Langemeyer, J., Codina, X., Gilabert, J., Guilera, N., Vidal, V., Segura, R., and Villalba, G. “A take-home message from COVID-19 on urban air pollution reduction through mobility limitations and teleworking”. *npj urban sustainability* 1.35 (2021). DOI: <https://doi.org/10.1038/s42949-021-00037-7>.
- [5] Bauer, P., Thorpe, A., and Brunet, G. “The quiet revolution of numerical weather prediction.” *Nature* 525 (2015), pp. 47–55. DOI: <https://doi.org/10.1038/nature14956>.
- [6] Beirle, S., Platt, U., Wenig, M., and Wagner, T. “Weekly cycle of NO₂ by GOME measurements: a signature of anthropogenic sources”. *Atmospheric Chemistry and Physics* 3.6 (Dec. 2003), pp. 2225–2232. DOI: 10.5194/acp-3-2225-2003.
- [7] Bjerknes, V. “Meteorology as an exact science”. *Monthly Weather Review* 42.1 (1914), pp. 11–14. DOI: 10.1175/1520-0493(1914)42<11:maaes>2.0.co;2.
- [8] Bonekamp, P. N. J., Collier, E., and Immerzeel, W. W. “The Impact of Spatial Resolution, Land Use, and Spinup Time on Resolving Spatial Precipitation Patterns in the Himalayas”. *Journal of Hydrometeorology* 19.10 (2018), pp. 1565–1581. DOI: 10.1175/jhm-d-17-0212.1.

- [9] Brasseur, G. P. and Jacob, D. J. “Modeling of Atmospheric Chemistry”. Cambridge University Press, (2017). DOI: 10.1017/9781316544754.
- [10] Bremen Airport. “Unternehmen Flughafen - Wir schaffen Verbindungen. Zahlen & Fakten”. (2022). URL: <https://www.bremen-airport.com/unternehmen/flughafen-bremen/zahlen-und-fakten> (visited on 6.8.2022).
- [11] Bremen Airport. “ZAHLEN & FAKTEN - Verkehrsstatistik Juni 2022”. (2022). URL: https://www.bremen-airport.com/fileadmin/user_upload/Monatsbericht_extern_Juni_2022.pdf (visited on 11.10.2022).
- [12] Brioude, J., Arnold, D., Stohl, A., Cassiani, M., Morton, D., Seibert, P., Angevine, W., Evan, S., Dingwell, A., Fast, J. D., Easter, R. C., Pisso, I., Burkhardt, J., and Wotawa, G. “The Lagrangian particle dispersion model FLEXPART-WRF version 3.1”. *Geoscientific Model Development* 6.6 (2013), pp. 1889–1904. DOI: 10.5194/gmd-6-1889-2013.
- [13] Brunekeef, B. “Air pollution and life expectancy: is there a relation?” *Occupational and Environmental Medicine* 54.11 (1997), pp. 781–784. ISSN: 1351-0711. DOI: 10.1136/oem.54.11.781.
- [14] Brunekeef, B. and Holgate, T. S. “Air pollution and health”. *The Lancet* 360.9341 (2002), pp. 1233–1242. DOI: [https://doi.org/10.1016/S0140-6736\(02\)11274-8](https://doi.org/10.1016/S0140-6736(02)11274-8).
- [15] Cécé, R., Bernard, D., Brioude, J., and Zahibo, N. “Microscale anthropogenic pollution modelling in a small tropical island during weak trade winds: Lagrangian particle dispersion simulations using real nested LES meteorological fields”. *Atmospheric Environment* 139 (2016), pp. 98–112. DOI: 10.1016/j.atmosenv.2016.05.028.
- [16] Copernicus Sentinel-5P (processed by European Space Agency). “TROPOMI Level 2 Nitrogen Dioxide total column products. Version 02.” (2021). DOI: <https://doi.org/10.5270/S5P-9bnp8q8>.
- [17] Cornu, A. M. “II. Sur la limite ultraviolette du spectre solaire”. *Proceedings of the Royal Society of London* 29.196-199 (1879), pp. 47–55. DOI: 10.1098/rsp1.1879.0011.
- [18] Crippa, M., Solazzo, E., Huang, G., Guizzardi, D., Koffi, E., Muntean, M., Schieberle, C., Friedrich, R., and Janssens-Maenhout, G. “High resolution temporal profiles in the Emissions Database for Global Atmospheric Research”. *Scientific Data* 7 (2020). DOI: 10.1038/s41597-020-0462-2.
- [19] Cuo, L., Pagano, T. C., and Wang, Q. J. “A Review of Quantitative Precipitation Forecasts and Their Use in Short- to Medium-Range Streamflow Forecasting”. *Journal of Hydrometeorology* 12.5 (2011), pp. 713–728. DOI: 10.1175/2011jhm1347.1.

-
- [20] Danckaert, T., Fayt, C., Roozendael, M. van, Smedt, I. de, Letocart, V., Merlaud, A., and Pinardi, G. “QDOAS Software user manual - Version 3.2”. Royal Belgian Institute for Space Aeronomy. (2017). URL: https://uv-vis.aeronomie.be/software/QDOAS/QDOAS_manual.pdf.
- [21] Darras, S., Granier, C., Pignot, V., Bodichon, R., Boonne, C., Lioussé, C., and Paulin, M. “ECCAD: Emission of Atmospheric Compounds & Compilation of Ancillary Data”. *AGU Fall Meeting Abstracts* (2010).
- [22] Demtröder, W. “Experimentalphysik 2 - Elektrizität und Optik”. Springer-Verlag, (2017). DOI: 10.1007/978-3-662-55790-7. URL: <https://doi.org/10.1007/978-3-662-55790-7>.
- [23] Demtröder, W. “Experimentalphysik 3 - Atome, Moleküle und Festkörper”. Springer-Verlag, (2016). DOI: 10.1007/978-3-662-49094-5. URL: <https://doi.org/10.1007/978-3-662-49094-5>.
- [24] Dodge, M. “Combined use of modeling techniques and smog chamber data to derive ozone - precursor relationships”. *Proceedings of the international conference on photochemical oxidant pollution and its control*. Ed. by B. Dimitriades. Vol. 2. B. U.S. Environmental Protection Agency, (1977), pp. 881–889. URL: https://hero.epa.gov/hero/index.cfm/reference/details/reference_id/38646.
- [25] Dudhia, J. “Numerical Study of Convection Observed during the Winter Monsoon Experiment Using a Mesoscale Two-Dimensional Model”. *Journal of Atmospheric Sciences* 46.20 (1989), pp. 3077–3107. DOI: 10.1175/1520-0469(1989)046<3077:NSOCOD>2.0.CO;2.
- [26] DWD. “Surface weather observations”. (2022). URL: https://www.dwd.de/EN/ourservices/surface_weather_observations/surface_weather_observations.html (visited on 12.9.2022).
- [27] DWD Climate Data Center (CDC). “Recent hourly station observations of 2m air temperature and humidity for Germany, quality control not completed yet, version recent”. (2022). URL: https://opendata.dwd.de/climate_environment/CDC/observations_germany/climate/hourly/air_temperature/recent/ (visited on 31.7.2022).
- [28] DWD Climate Data Center (CDC). “Recent hourly station observations of precipitation for Germany, quality control not completed yet, version recent”. (2022). URL: https://opendata.dwd.de/climate_environment/CDC/observations_germany/climate/hourly/precipitation/recent/ (visited on 31.7.2022).
- [29] DWD Climate Data Center (CDC). “Recent hourly station observations of wind speed and wind direction for Germany, quality control not completed yet, version recent”. (2022). URL: <https://opendata.dwd.de/>
-

- climate_environment/CDC/observations_germany/climate/hourly/wind/recent/ (visited on 31.7.2022).
- [30] ECMWF. “ERA5: data documentation”. (2022). URL: <https://confluence.ecmwf.int/display/CKB/ERA5:+data+documentation> (visited on 31.7.2022).
- [31] Emberson, L. “Effects of ozone on agriculture, forests and grasslands”. *Philosophical Transactions of the Royal Society A: Mathematical, Physical and Engineering Sciences* 378.2183 (Sept. 2020), p. 20190327. DOI: 10.1098/rsta.2019.0327.
- [32] Emmons, L. K., Walters, S., Hess, P. G., Lamarque, J.-F., Pfister, G. G., Fillmore, D., Granier, C., Guenther, A., Kinnison, D., Laepple, T., Orlando, J., Tie, X., Tyndall, G., Wiedinmyer, C., Baughcum, S. L., and Kloster, S. “Description and evaluation of the Model for Ozone and Related chemical Tracers, version 4 (MOZART-4)”. *Geoscientific Model Development* 3.1 (2010), pp. 43–67. DOI: 10.5194/gmd-3-43-2010.
- [33] Faustini, A., Rapp, R., and Forastiere, F. “Nitrogen dioxide and mortality: review and meta-analysis of long-term studies”. *European Respiratory Journal* 44.3 (2014), pp. 744–753. ISSN: 0903-1936. DOI: 10.1183/09031936.00114713.
- [34] Georgiou, G. K., Christoudias, T., Proestos, Y., Kushta, J., Hadjinicolaou, P., and Lelieveld, J. “Air quality modelling in the summer over the eastern Mediterranean using WRF-Chem: chemistry and aerosol mechanism inter-comparison”. *Atmospheric Chemistry and Physics* 18.3 (2018), pp. 1555–1571. DOI: 10.5194/acp-18-1555-2018.
- [35] Granier, C., Darras, S., Gon, H. D. van der, Doubalova, J., Elguindi, N., Galle, B., Gauss, M., Guevara, M., Jalkanen, J.-P., Kuenen, J., Lioussé, C., Quack, B., Simpson, D., and Sindelarova, K. “The Copernicus Atmosphere Monitoring Service global and regional emissions” (2019). DOI: 10.24380/d0bn-kx16.
- [36] Grell, G. A. “Prognostic Evaluation of Assumptions Used by Cumulus Parameterizations”. *Monthly Weather Review* 121.3 (1993), pp. 764–787. DOI: 10.1175/1520-0493(1993)121<0764:PEOAU>2.0.CO;2.
- [37] Grell, G. A. and Dévényi, D. “A generalized approach to parameterizing convection combining ensemble and data assimilation techniques”. *Geophysical Research Letters* 29.14 (2002), pp. 38-1-38-4. DOI: <https://doi.org/10.1029/2002GL015311>.
- [38] Grell, G. A., Dudhia, J., and Stauffer, D. R. “A Description of the Fifth-Generation Penn State/NCAR Mesoscale Model (MM5)”. NCAR Technical Note. National Center for Atmospheric Research. (1995).

-
- [39] Grell, G. A., Peckham, S. E., Schmitz, R., McKeen, S. A., Frost, G., Skamarock, W. C., and Eder, B. “Fully coupled “online” chemistry within the WRF model”. *Atmospheric Environment* 39.37 (2005), pp. 6957–6975. ISSN: 1352-2310. DOI: <https://doi.org/10.1016/j.atmosenv.2005.04.027>.
- [40] Guenther, A. B., Jiang, X., Heald, C. L., Sakulyanontvittaya, T., Duhl, T., Emmons, L. K., and Wang, X. “The Model of Emissions of Gases and Aerosols from Nature version 2.1 (MEGAN2.1): an extended and updated framework for modeling biogenic emissions”. *Geoscientific Model Development* 5.6 (2012), pp. 1471–1492. DOI: 10.5194/gmd-5-1471-2012.
- [41] Guevara, M., Tena, C., Porquet, M., Jorba, O., and Pérez García-Pando, C. “HERMESv3, a stand-alone multi-scale atmospheric emission modelling framework – Part 1: global and regional module”. *Geoscientific Model Development* 12.5 (2019), pp. 1885–1907. DOI: 10.5194/gmd-12-1885-2019.
- [42] Haken, H. and Wolf, H. C. “Molekülphysik und Quantenchemie”. Springer Berlin Heidelberg, (2003). DOI: 10.1007/978-3-662-08826-5. URL: <https://doi.org/10.1007/978-3-662-08826-5>.
- [43] Hanna, S. R. and Yang, R. “Evaluations of Mesoscale Models’ Simulations of Near-Surface Winds, Temperature Gradients, and Mixing Depths”. *Journal of Applied Meteorology* 40.6 (2001), pp. 1095–1104. DOI: 10.1175/1520-0450(2001)040<1095:eommso>2.0.co;2.
- [44] Hilboll, A., Richter, A., and Burrows, J. P. “Supplementary material to “Long-term changes of tropospheric NO₂ over megacities derived from multiple satellite instruments””. *Atmospheric Chemistry and Physics* 13.8 (2013), pp. 4145–4169. DOI: 10.5194/acp-13-4145-2013.
- [45] Hong, S.-Y., Noh, Y., and Dudhia, J. “A New Vertical Diffusion Package with an Explicit Treatment of Entrainment Processes”. *Monthly Weather Review* 134.9 (2006), pp. 2318–2341. DOI: 10.1175/MWR3199.1.
- [46] Hönninger, G. “Ground-based measurements of halogen oxides at the Hudson Bay by active longpath DOAS and passive MAX-DOAS”. *Geophysical Research Letters* 31.4 (2004). DOI: 10.1029/2003gl018982.
- [47] Hu, Z., Zhao, C., Huang, J., Leung, L. R., Qian, Y., Yu, H., Huang, L., and Kalashnikova, O. V. “Trans-Pacific transport and evolution of aerosols: evaluation of quasi-global WRF-Chem simulation with multiple observations”. *Geoscientific Model Development* 9.5 (2016), pp. 1725–1746. DOI: 10.5194/gmd-9-1725-2016.
- [48] Huijnen, V., Eskes, H. J., Poupkou, A., Elbern, H., Boersma, K. F., Foret, G., Sofiev, M., Valdebenito, A., Flemming, J., Stein, O., Gross, A., Robertson, L., D’Isidoro, M., Kioutsioukis, I., Friese, E., Amstrup, B., Bergstrom, R., Strunk, A., Vira, J., Zyryanov, D., Maurizi, A., Melas, D., Peuch, V.-H., and
-

- Zerefos, C. “Comparison of OMI NO₂ tropospheric columns with an ensemble of global and European regional air quality models”. *Atmospheric Chemistry and Physics* 10.7 (2010), pp. 3273–3296. DOI: 10.5194/acp-10-3273-2010.
- [49] Ibrahim, O., Shaiganfar, R., Sinreich, R., Stein, T., Platt, U., and Wagner, T. “Car MAX-DOAS measurements around entire cities: quantification of NO_x emissions from the cities of Mannheim and Ludwigshafen (Germany)”. *Atmospheric Measurement Techniques* 3.3 (2010), pp. 709–721. DOI: 10.5194/amt-3-709-2010.
- [50] Jiménez, P. A., Dudhia, J., González-Rouco, J. F., Navarro, J., Montávez, J. P., and García-Bustamante, E. “A Revised Scheme for the WRF Surface Layer Formulation”. *Monthly Weather Review* 140.3 (2012), pp. 898–918. DOI: 10.1175/MWR-D-11-00056.1.
- [51] Johansson, M., Galle, B., Yu, T., Tang, L., Chen, D., Li, H., Li, J. X., and Zhang, Y. “Quantification of total emission of air pollutants from Beijing using mobile mini-DOAS”. *Atmospheric Environment* 42.29 (2008), pp. 6926–6933. ISSN: 1352-2310. DOI: <https://doi.org/10.1016/j.atmosenv.2008.05.025>.
- [52] Khan, I., Shah, D., and Shah, S. S. “COVID-19 pandemic and its positive impacts on environment: an updated review”. *International Journal of Environmental Science and Technology* 18.2 (2020), pp. 521–530. DOI: 10.1007/s13762-020-03021-3.
- [53] Kleczek, M. A., Steeneveld, G.-J., and Holtslag, A. A. M. “Evaluation of the Weather Research and Forecasting Mesoscale Model for GABLS3: Impact of Boundary-Layer Schemes, Boundary Conditions and Spin-Up”. *Boundary-Layer Meteorology* 152.2 (2014), pp. 213–243. DOI: 10.1007/s10546-014-9925-3.
- [54] Kurucz, R. L., Furenlid, I., Brault, J., and Testerman, L. “Solar flux atlas from 296 to 1300 nm”. National Solar Observatory Atlas No. 1. (1984).
- [55] Lamsal, L. N., Martin, R. V., Donkelaar, A. van, Celarier, E. A., Bucsela, E. J., Boersma, K. F., Dirksen, R., Luo, C., and Wang, Y. “Indirect validation of tropospheric nitrogen dioxide retrieved from the OMI satellite instrument: Insight into the seasonal variation of nitrogen oxides at northern mid-latitudes”. *Journal of Geophysical Research* 115.D5 (2010). DOI: 10.1029/2009jd013351.
- [56] Lee, H.-J., Kim, S.-W., Brioude, J., Cooper, O. R., Frost, G. J., Kim, C.-H., Park, R. J., Trainer, M., and Woo, J.-H. “Transport of NO_x in East Asia identified by satellite and in situ measurements and Lagrangian particle dispersion model simulations”. *Journal of Geophysical Research: Atmospheres* 119.5 (2014), pp. 2574–2596. DOI: 10.1002/2013jd021185.

-
- [57] Lelieveld, J. and Crutzen, P. J. “Influences of cloud photochemical processes on tropospheric ozone”. *Nature* 343 (1990), pp. 227–233.
- [58] Lin, J. C. “Lagrangian Modeling of the Atmosphere: An Introduction”. American Geophysical Union, (2013), pp. 1–11. DOI: 10.1029/2012gm001376. URL: <https://doi.org/10.1029/2012gm001376>.
- [59] Madronich, S. “Photodissociation in the atmosphere: 1. Actinic flux and the effects of ground reflections and clouds”. *Journal of Geophysical Research* 92.D8 (1987), p. 9740. DOI: 10.1029/jd092id08p09740.
- [60] Madronich, S. and Weller, G. “Numerical Integration Errors in Calculated Tropospheric Photodissociation Rate Coefficients”. *Journal of Atmospheric Chemistry* 10 (1990), pp. 289–300.
- [61] Marsh, D., Mills, M., Kinnison, D. E., and Lamarque, J. -. “Climate change from 1850 to 2005 simulated in CESM1(WACCM)”. *Journal Of Climate*, 26, 7372-7391 (2013). DOI: 10.1175/JCLI-D-12-00558.1.
- [62] Miguez-Macho, G., Stenchikov, G. L., and Robock, A. “Spectral nudging to eliminate the effects of domain position and geometry in regional climate model simulations”. *Journal of Geophysical Research: Atmospheres* 109.D13 (2004). DOI: <https://doi.org/10.1029/2003JD004495>.
- [63] Mlawer, E. J., Taubman, S. J., Brown, P. D., Iacono, M. J., and Clough, S. A. “Radiative transfer for inhomogeneous atmospheres: RRTM, a validated correlated-k model for the longwave”. *Journal of Geophysical Research: Atmospheres* 102.D14 (1997), pp. 16663–16682. DOI: <https://doi.org/10.1029/97JD00237>.
- [64] Morrison, H., Thompson, G., and Tatarskii, V. “Impact of Cloud Microphysics on the Development of Trailing Stratiform Precipitation in a Simulated Squall Line: Comparison of One- and Two-Moment Schemes”. *Monthly Weather Review* 137.3 (2009), pp. 991–1007. DOI: 10.1175/2008MWR2556.1.
- [65] National Research Council. “Rethinking the Ozone Problem in Urban and Regional Air Pollution”. National Academies Press, (1991). DOI: 10.17226/1889. URL: <https://doi.org/10.17226/1889>.
- [66] NCAR. “Download WRF-Chem Processors”. (2015). URL: <https://www.aom.ucar.edu/wrf-chem/download.shtml> (visited on 31.7.2022).
- [67] NCAR. “Tropospheric Ultraviolet and Visible (TUV) Radiation Model”. (2022). URL: <https://www2.aom.ucar.edu/modeling/tropospheric-ultraviolet-and-visible-tuv-radiation-model> (visited on 9.10.2022).
- [68] NCAR. “WRF-Chem Tools for the Community”. (2022). URL: <https://www2.aom.ucar.edu/wrf-chem/wrf-chem-tools-community> (visited on 5.11.2022).
-

- [69] Neuman, J. A., Parrish, D. D., Trainer, M., Ryerson, T. B., Holloway, J. S., Nowak, J. B., Swanson, A., Flocke, F., Roberts, J. M., Brown, S. S., Stark, H., Sommariva, R., Stohl, A., Peltier, R., Weber, R., Wollny, A. G., Sueper, D. T., Hubler, G., and Fehsenfeld, F. C. “Reactive nitrogen transport and photochemistry in urban plumes over the North Atlantic Ocean”. *Journal of Geophysical Research: Atmospheres* 111.D23 (Aug. 2006). DOI: 10.1029/2005jd007010.
- [70] Novakov, T. and Penner, J. E. “Large contribution of organic aerosols to cloud-condensation-nuclei concentrations”. *Nature* 365 (1993), pp. 823–826.
- [71] Nunnermacker, L. J., Kleinman, L. I., Imre, D., Daum, P. H., Lee, Y.-N., Lee, J. H., Springston, S. R., Newman, L., and Gillani, N. “NO_y lifetimes and O₃ production efficiencies in urban and power plant plumes: Analysis of field data”. *Journal of Geophysical Research: Atmospheres* 105.D7 (Apr. 2000), pp. 9165–9176. DOI: 10.1029/1999jd900753.
- [72] Peckham, S., Grell, G., McKeen, S., Ahmadov, R., Wong, K. Y., Barth, M., Pfister, G., Wiedinmyer, C., Fast, J., Gustafson, W., Ghan, S., Zaveri, R., Easter, R., Barnard, J., Chapman, E., Hewson, M., Schmitz, R., Salzmann, M., Beck, V., and Freitas, S. “WRF-Chem Version 3.8.1 User’s Guide”. National oceanic and atmospheric administration. (2017).
- [73] Platt, U. and Stutz, J. “Differential Absorption Spectroscopy”. *Physics of Earth and Space Environments*. Springer Berlin Heidelberg, (2008), pp. 135–174. DOI: 10.1007/978-3-540-75776-4_6. URL: https://doi.org/10.1007/978-3-540-75776-4_6.
- [74] Popp, C., Brunner, D., Damm, A., Van Roozendaal, M., Fayt, C., and Buchmann, B. “High-resolution NO₂ remote sensing from the Airborne Prism Experiment (APEX) imaging spectrometer”. *Atmospheric Measurement Techniques* 5.9 (2012), pp. 2211–2225. DOI: 10.5194/amt-5-2211-2012.
- [75] Powers, J. G., Klemp, J. B., Skamarock, W. C., Davis, C. A., Dudhia, J., Gill, D. O., Coen, J. L., Gochis, D. J., Ahmadov, R., Peckham, S. E., Grell, G. A., Michalakes, J., Trahan, S., Benjamin, S. G., Alexander, C. R., Dimego, G. J., Wang, W., Schwartz, C. S., Romine, G. S., Liu, Z., Snyder, C., Chen, F., Barlage, M. J., Yu, W., and Duda, M. G. “The Weather Research and Forecasting Model: Overview, System Efforts, and Future Directions”. *Bulletin of the American Meteorological Society* 98.8 (2017), pp. 1717–1737. DOI: 10.1175/BAMS-D-15-00308.1.
- [76] Release, P. and Register, T. “swb Entsorgung GmbH & Co. KG / MHKW Bremen”. (2020). URL: <https://thru.de/> (visited on 11.9.2022).

-
- [77] Richter. “Absorptionsspektroskopische Messungen Stratosphärischer Spurengase über Bremen”. PhD thesis. University of Bremen, (1997). URL: http://www.iup.uni-bremen.de/doas/paper/diss_97_richter.zip.
- [78] Richter, A., Begoin, M., Hilboll, A., and Burrows, J. P. “An improved NO₂ retrieval for the GOME-2 satellite instrument”. *Atmospheric Measurement Techniques* 4.6 (June 2011), pp. 1147–1159. DOI: 10.5194/amt-4-1147-2011.
- [79] Rozanov, V., Rozanov, A., Kokhanovsky, A., and Burrows, J. “Radiative transfer through terrestrial atmosphere and ocean: Software package SCIA-TRAN.” *J. Quant. Spec. R. Trans.* 133 (2014), pp. 13–71. DOI: 10.1016/j.jqsrt.2013.07.004.
- [80] Ryerson, T. B. “Effect of petrochemical industrial emissions of reactive alkenes and NO_x on tropospheric ozone formation in Houston, Texas”. *Journal of Geophysical Research* 108.D8 (2003). DOI: 10.1029/2002jd003070.
- [81] Schaub, D., Brunner, D., Boersma, K. F., Keller, J., Folini, D., Buchmann, B., Berresheim, H., and Staehelin, J. “SCIAMACHY tropospheric NO₂ over Switzerland: estimates of NO_x lifetimes and impact of the complex Alpine topography on the retrieval”. *Atmospheric Chemistry and Physics* 7.23 (Dec. 2007), pp. 5971–5987. DOI: 10.5194/acp-7-5971-2007.
- [82] Schönhardt, A., Altube, P., Gerilowski, K., Krautwurst, S., Hartmann, J., Meier, A. C., Richter, A., and Burrows, J. P. “A wide field-of-view imaging DOAS instrument for two-dimensional trace gas mapping from aircraft”. *Atmospheric Measurement Techniques* 8.12 (Dec. 2015), pp. 5113–5131. DOI: 10.5194/amt-8-5113-2015.
- [83] Schreier, S. F., Richter, A., and Burrows, J. P. “Near-surface and path-averaged mixing ratios of NO₂ derived from car DOAS zenith-sky and tower DOAS off-axis measurements in Vienna: a case study”. *Atmospheric Chemistry and Physics* 19.9 (2019), pp. 5853–5879. DOI: 10.5194/acp-19-5853-2019.
- [84] Serdyuchenko, A., Gorshelev, V., Weber, M., Chehade, W., and Burrows, J. P. “High spectral resolution ozone absorption cross-sections - Part 2: Temperature dependence”. *Atmospheric Measurement Techniques* 7.2 (2014), pp. 625–636. DOI: 10.5194/amt-7-625-2014.
- [85] Seyler, A., Meier, A. C., Wittrock, F., Kattner, L., Mathieu-Üffing, B., Peters, E., Richter, A., Ruetz, T., Schönhardt, A., Schmolke, S., and Burrows, J. P. “Studies of the horizontal inhomogeneities in NO₂ concentrations above a shipping lane using ground-based multi-axis differential optical absorption spectroscopy (MAX-DOAS) measurements and validation with airborne

- imaging DOAS measurements”. *Atmospheric Measurement Techniques* 12.11 (2019), pp. 5959–5977. DOI: 10.5194/amt-12-5959-2019.
- [86] Seyler, A. “Investigating air quality in the marine environment of the North and Baltic Sea with MAX-DOAS measurements”. PhD thesis. University of Bremen, (2020). URL: <https://media.suub.uni-bremen.de/handle/elib/5053>.
- [87] Shah, V., Jacob, D. J., Li, K., Silvern, R. F., Zhai, S., Liu, M., Lin, J., and Zhang, Q. “Effect of changing NO_x lifetime on the seasonality and long-term trends of satellite-observed tropospheric NO₂ columns over China”. *Atmospheric Chemistry and Physics* 20.3 (2020), pp. 1483–1495. DOI: 10.5194/acp-20-1483-2020.
- [88] Shaiganfar, R., Beirle, S., Sharma, M., Chauhan, A., Singh, R. P., and Wagner, T. “Estimation of NO_x emissions from Delhi using Car MAX-DOAS observations and comparison with OMI satellite data”. *Atmospheric Chemistry and Physics* 11.21 (2011), pp. 10871–10887. DOI: 10.5194/acp-11-10871-2011.
- [89] Skamarock, W. C., Klemp, J. B., Dudhia, J., Gill, D. O., Liu, Z., Berner, J., Wang, W., Powers, J. G., Duda, M. G., and Barker D. M. Huang, X. “A Description of the Advanced Research WRF Model Version 4.1 (No. NCAR/TN-556+STR)” (2019). DOI: 10.5065/1dfh-6p97.
- [90] Solomon, S., Schmeltekopf, A. L., and Sanders, R. W. “On the interpretation of zenith sky absorption measurements”. *Journal of Geophysical Research: Atmospheres* 92.D7 (1987), pp. 8311–8319. DOI: <https://doi.org/10.1029/JD092iD07p08311>.
- [91] Spicer, C. W. “Nitrogen Oxide Reactions in the Urban Plume of Boston”. *Science* 215.4536 (Feb. 1982), pp. 1095–1097. DOI: 10.1126/science.215.4536.1095.
- [92] Stohl, A., Forster, C., Frank, A., Seibert, P., and Wotawa, G. “Technical note: The Lagrangian particle dispersion model FLEXPART version 6.2”. *Atmospheric Chemistry and Physics* 5.9 (2005), pp. 2461–2474. DOI: 10.5194/acp-5-2461-2005.
- [93] Stohl, A., Sodemann, H., Eckhardt, S., Frank, A., Seibert, P., and Wotawa, G. “The Lagrangian particle dispersion model FLEXPART version 8.2”. (2010). URL: <https://www.flexpart.eu/> (visited on 26.8.2022).
- [94] Storch, H. von, Langenberg, H., and Feser, F. “A Spectral Nudging Technique for Dynamical Downscaling Purposes”. *Monthly Weather Review* 128.10 (2000), pp. 3664–3673. DOI: 10.1175/1520-0493(2000)128<3664:asntfd>2.0.co;2.

- [95] swb. “Unsere Müllverbrennungsanlagen in Bremen”. (2022). URL: <https://www.swb.de/geschaeftskunden/entsorgung/anlagen> (visited on 6.8.2022).
- [96] Tewari, M., Chen, F., Wang, W., Dudhia, J., LeMone, M. A., Mitchell, K. E., Ek, M., Gayno, G., Wegiel, J., and Cuenca, R. “Implementation and verification of the unified Noah land-surface model in the WRF model”. In *20th Conference on Weather Analysis and Forecasting/16th Conference on Numerical Weather Prediction. American Meteorological Society*. (2004).
- [97] Thalman, R. and Volkamer, R. “Temperature dependent absorption cross-sections of O₂-O₂ collision pairs between 340 and 630 nm and at atmospherically relevant pressure”. *Physical Chemistry Chemical Physics* 15.37 (2013), p. 15371. DOI: 10.1039/c3cp50968k.
- [98] Tie, X., Madronich, S., Li, G., Ying, Z., Zhang, R., Garcia, A. R., Lee-Taylor, J., and Liu, Y. “Characterizations of chemical oxidants in Mexico City: A regional chemical dynamical model (WRF-Chem) study”. *Atmospheric Environment* 41.9 (2007), pp. 1989–2008. DOI: 10.1016/j.atmosenv.2006.10.053.
- [99] Umweltbundesamt. “Air quality index”. (2022). URL: <https://www.umweltbundesamt.de/en/data/air/air-data/air-quality> (visited on 31.7.2022).
- [100] Umweltbundesamt. “EU-Meta-Stationen”. (2022). URL: <https://www.env-it.de/stationen/public/downloadRequest.do> (visited on 31.7.2022).
- [101] United Nations Educational, Scientific and Cultural Organization. “Environmental toxicology and human health”. Ed. by T. Satoh. Vol. 1. EOLSS, (2009).
- [102] United States Environmental Protection Agency. “NAAQS Table”. (2022). URL: <https://www.epa.gov/criteria-air-pollutants/naaqs-table> (visited on 6.11.2022).
- [103] United States Environmental Protection Agency. “National Ambient Air QualityStandards for Ozone”. (2015). URL: <https://www.govinfo.gov/content/pkg/FR-2015-10-26/pdf/2015-26594.pdf> (visited on 31.10.2022).
- [104] University of Wyoming. “Atmospheric Soundings”. (2022). URL: <http://weather.uwyo.edu/upperair/sounding.html> (visited on 31.7.2022).
- [105] Vandaele, A. C., Hermans, C., Simon, P. C., Roozendael, M. V., Guilmot, J. M., Carleer, M., and Colin, R. “Fourier transform measurement of NO₂ absorption cross-section in the visible range at room temperature”. *Journal of Atmospheric Chemistry* 25.3 (Nov. 1996), pp. 289–305. DOI: 10.1007/bf00053797.
- [106] Waldron, K. M., Paegle, J., and Horel, J. D. “Sensitivity of a Spectrally Filtered and Nudged Limited-Area Model to Outer Model Options”. *Monthly*

- Weather Review* 124.3 (1996), pp. 529–547. DOI: 10.1175/1520-0493(1996)124<0529:soasfa>2.0.co;2.
- [107] Wiedinmyer, C., Akagi, S. K., Yokelson, R. J., Emmons, L. K., Al-Saadi, J. A., Orlando, J. J., and Soja, A. J. “The Fire INventory from NCAR (FINN): a high resolution global model to estimate the emissions from open burning”. *Geoscientific Model Development* 4.3 (2011), pp. 625–641. DOI: 10.5194/gmd-4-625-2011.
- [108] Wittrock, F., Oetjen, H., Richter, A., Fietkau, S., Medeke, T., Rozanov, A., and Burrows, J. P. “MAX-DOAS measurements of atmospheric trace gases in Ny-Ålesund - Radiative transfer studies and their application”. *Atmospheric Chemistry and Physics* 4.4 (2004), pp. 955–966. DOI: 10.5194/acp-4-955-2004.
- [109] World Health Organization. “Air quality and health - Type of pollutants”. (2022). URL: <https://www.who.int/teams/environment-climate-change-and-health/air-quality-and-health/health-impacts/types-of-pollutants> (visited on 13.10.2022).
- [110] Zhang, J., Wei, Y., and Fang, Z. “Ozone Pollution: A Major Health Hazard Worldwide”. *Frontiers in Immunology* 10 (2019). ISSN: 1664-3224. DOI: 10.3389/fimmu.2019.02518.

Appendix

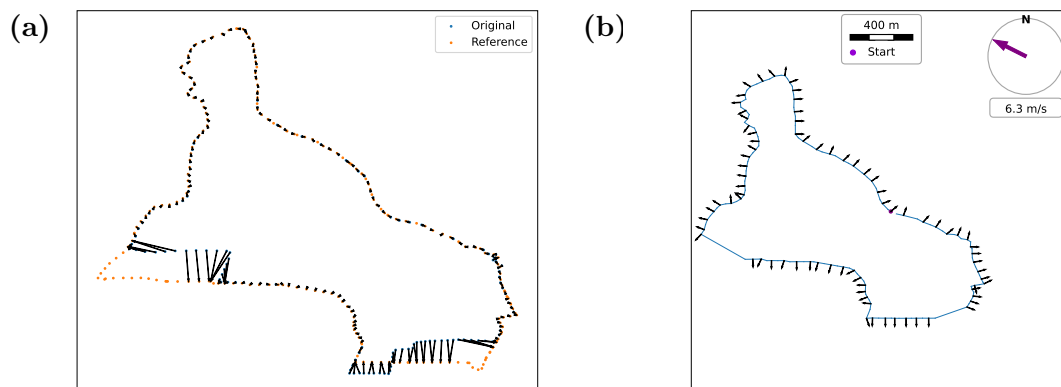


Figure 1: Two debugging figures to give some insights into the emission calculation implementation. **a)** Example for the projection of the driven round (blue) onto the ideal round (orange). The signal is moved to the closest point on the ideal round and averaged over if there are multiple values present. The arrows indicate the closest point. **b)** Visualization of the automatically calculated normal vectors for every second point on the round.

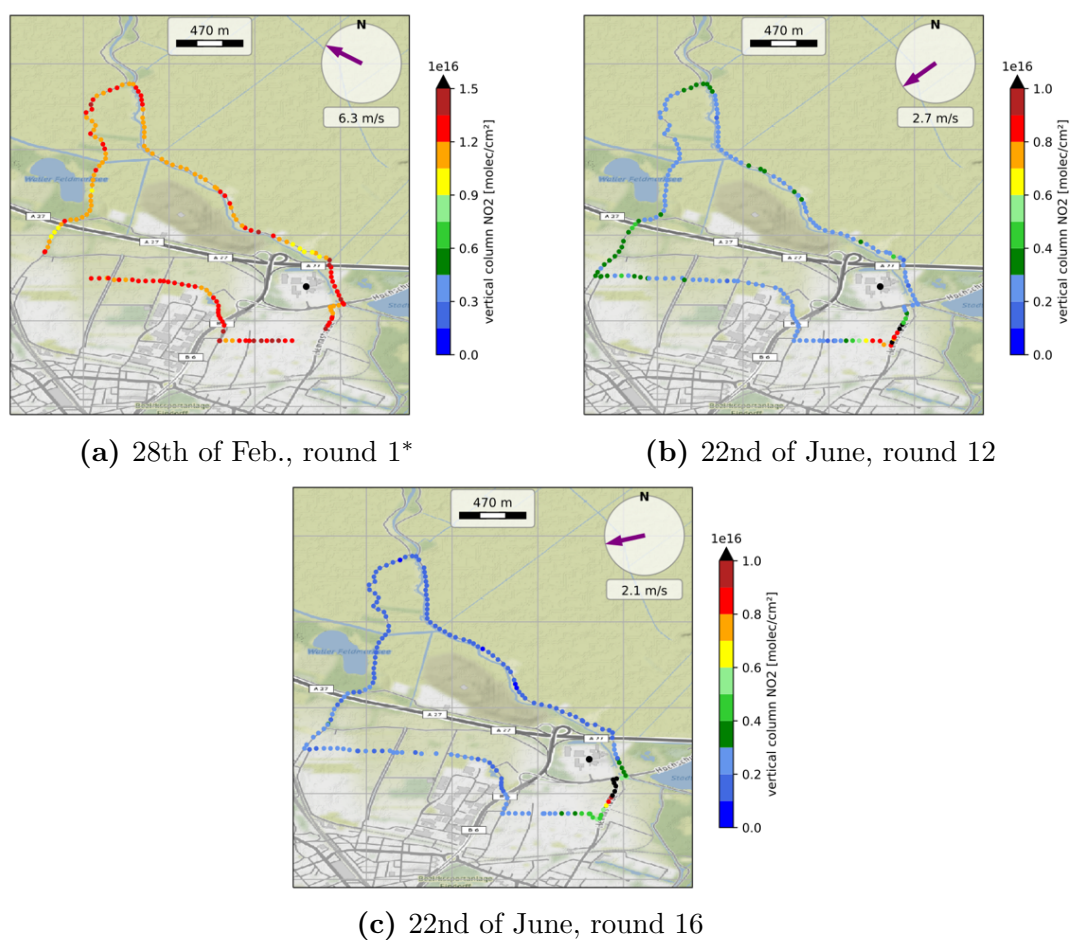


Figure 2: Overview of the rounds excluded from evaluation. **a)** Round 1 is excluded due to the signal dissipating to background levels. **b)** & **c)** Rounds 12 and 16 are excluded due to the wrong wind direction in the database. The upper limit of the color bar is modified for figures labeled with *.

Run Hermesv3_gr with WRF-Chem

Running Hermesv3_gr with WRF-Chem is possible but some additional steps are needed to make it work.

The options for running Hermes are found in *hermes.conf*. In that file, the output grid as well as the simulation period, file paths to profiles etc. are defined. The used configuration file is provided at the end.

Hermes and WRF are using different conventions to declare a grid. Where WRF is using the center point of a domain, Hermes is declaring a grid via the bottom left grid point. The different attributes can be read out from a wrfinput file. The following dictionary helps to switch between the conventions for the Lambert Conformal Conic projection.

```
HERMES_TO_WRF_ATTRS = {
  "lat_1": "TRUELAT1",
  "lat_2": "TRUELAT2",
  "lon_0": "STANDLON",
  "lat_0": "MOAD_CEN_LAT",
  "nx": "WEST-EAST_PATCHEND_UNSTAG",
  "ny": "SOUTH-NORTHPATCHEND_UNSTAG",
  "inc_x": "DX",
  "inc_y": "DY",
  "x_0": x_0,
  "y_0": y_0
}
```

`x_0` & `y_0` do not have an equivalent property from the wrfinput file. They represent the x- and y-distance from the center to the bottom left point in meters and can be returned with the help of the pyproj package. Because the output of Hermes does not contain longitude and latitude, one can check whether the gridding was successful by using the latitude and longitude from

`hermesv3_gr/data/auxiliar_files/<yourgrid>/temporal_coords.nc`.

The rest of Hermes is operated as usual. Possible country-specific and sector-specific diurnal cycles can be found at Crippa et al.¹. These however use the convention of daily weighting values ($\sum_i^N d_i = 1$), which need to be converted to Hermes conven-

¹Crippa, M. et al. "High resolution temporal profiles in the Emissions Database for Global Atmospheric Research". *Scientific Data* 7 (2020). DOI: 10.1038/s41597-020-0462-2

tion of hourly weighting values ($\sum_i^N h_i = 24$) by

$$h_j = \frac{d_j}{\frac{1}{N} \sum_i^N d_i}.$$

To ensure, that the output files from Hermes are processed correctly from WRF-Chem, two options have to be added to the namelist.

```
&time_control
...
auxinput5_interval_m           = 60,
frames_per_auxinput5          = 24,
\
```

The first option states that the data is available in hourly values. The second states that there are 24 timesteps (with typical settings: one day) in each Hermes file.

Furthermore, the Hermes output has to be renamed to match the convention from anthro_emis.

```
Hermesv3_d<domain>_YYYYMMDDHH.nc
      ↓
wrfchemi_d<domain>_YYYY-mm-DD_HH:MM:SS
```

This can be solved by linking the Hermes files with the new filenames to the directory of WRF-Chem. Afterward, WRF-Chem should run with the new anthropogenic emissions preprocessed by Hermes.

Configuration files

Listing 1: namelist.input

```

1 | !namelist.input.chem
2 | &time_control
3 |   force_use_old_data           =   T,
4 |   run_days                     =  47,
5 |   run_hours                     =   0,
6 |   run_minutes                   =   0,
7 |   run_seconds                   =   0,
8 |   start_year                    = 2022, 2022, 2022,
9 |   start_month                   =   05,   05,   05,
10 |  start_day                      =   15,   15,   15,
11 |  start_hour                     =   00,   00,   00,
12 |  start_minute                   =   00,   00,   00,
13 |  start_second                   =   00,   00,   00,
14 |  end_year                       = 2022, 2022, 2022,
15 |  end_month                      =   07,   07,   07,
16 |  end_day                       =   01,   01,   01,
17 |  end_hour                      =   00,   00,   00,
18 |  end_minute                    =   00,   00,   00,
19 |  end_second                    =   00,   00,   00,
20 |  debug_level                    =   0,
21 |
22 | !HISTORY OPTIONS
23 | history_interval                =  60,  60,  60,
24 | history_outname                 = 'path_to_wrfout/wrfout_d<domain>.<date>',
25 | frames_per_outfile              =  24,  24,  24,
26 | io_form_history                 =   2,
27 |
28 | !RESTART OPTIONS
29 | restart                        = .false.,
30 | write_hist_at_0h_rst           = .true.,
31 | restart_interval                = 10080,
32 | io_form_restart                 =   2,
33 | rst_outname                    = 'path_to_wrfirst/wrfirst_d<domain>.<date>',
34 |
35 | !INPUT OPTIONS
36 | auxinput1.inname               = 'path_to_met_em/met_em.d<domain>.<date>',
37 | io_form_input                   =   2,
38 | io_form_boundary                =   2,
39 | input_from_file                 = .true., .true., .true.,
40 | interval_seconds                = 3600,
41 | io_form_auxinput2              =   2,
42 |
43 | !PREPROCESSORS
44 | !Anthro Emis/Hermes
45 | auxinput5.interval_m           =  60,
46 | frames_per_auxinput5           =  24,
47 | io_form_auxinput5              =   2,
48 | !Bio Emis
49 | io_form_auxinput6              =   2,
50 | auxinput6.inname               = 'path_to_preprocessor_output/wrfbiochemi_d<
    domain>',
51 | !Fire Emis
52 | io_form_auxinput7              =   2,
53 | auxinput7.inname               = 'path_to_preprocessor_output/wrfirechemi_d<
    domain>.<date>',

```

```
54 |
55 | !Previous Simulation for Initialization of Chemistry
56 | !io_form_auxinput12           = 0,
57 | !auxinput12_inname           = 'wrf_chem_input',
58 | /
59 |
60 | &dfi_control
61 | /
62 |
63 | &domains
64 |   time_step                   = 180,
65 |   time_step_fract_num         = 0,
66 |   time_step_fract_den         = 1,
67 |   max_dom                     = 2,
68 |   s_we                        = 1, 1, 1,
69 |   e_we                        = 61, 91, 100,
70 |   s_sn                        = 1, 1, 1,
71 |   e_sn                        = 61, 91, 100,
72 |   e_vert                      = 33, 33, 33,
73 |   num_metgrid_levels          = 138,
74 |   num_metgrid_soil_levels     = 3,
75 |   dx                          = 30000,
76 |   dy                          = 30000,
77 |   grid_id                     = 1, 2, 3,
78 |   parent_id                   = 0, 1, 2,
79 |   i_parent_start              = 1, 17, 25,
80 |   j_parent_start              = 1, 14, 40,
81 |   parent_grid_ratio           = 1, 3, 3,
82 |   parent_time_step_ratio      = 1, 5, 3,
83 |   p_top_requested             = 5000,
84 |   feedback                    = 0,
85 |   smooth_option               = 0,
86 |   p_top_requested             = 5000,
87 |   zap_close_levels            = 50,
88 |   interp_type                 = 1,
89 |   t_extrap_type               = 2,
90 |   force_sfc_in_vinterp        = 0,
91 |   use_levels_below_ground     = .true.,
92 |   use_surface                 = .true.,
93 |   lagrange_order              = 1,
94 | /
95 |
96 | &physics
97 |   num_land_cat                = 21,
98 |   mp_physics                  = 10, 10, 10,
99 |   progn                       = 1, 1, 1,
100 |  ra_lw_physics                = 1, 1, 1,
101 |  ra_sw_physics                = 1, 1, 1,
102 |  radt                         = 30, 30, 30,
103 |  sf_sfclay_physics           = 1, 1, 1,
104 |  sf_surface_physics          = 2, 2, 2,
105 |  bl_pbl_physics              = 1, 1, 1,
106 |  bldt                         = 0, 0, 0,
107 |  cu_physics                   = 5, 5, 5,
108 |  cu_diag                      = 1,
109 |  cudt                         = 0, 0, 0,
110 |  ishallow                     = 0,
111 |  isfflx                       = 1,
112 |  ifsnow                       = 1,
```

```

113 icloud = 1,
114 surface_input_source = 1,
115 num_soil_layers = 4,
116 sf_urban_physics = 0,
117 mp_zero_out = 2,
118 mp_zero_out_thresh = 1.e-12,
119 maxiens = 1,
120 maxens = 3,
121 maxens2 = 3,
122 maxens3 = 16,
123 ensdim = 144,
124 cu_rad_feedback = .true.,
125 ! For SST !
126 !sst_update = 1,
127
128 /
129
130
131 &fdda
132 grid_fdda = 2, 0, 0,
133 gfdda_inname = "wrffdda_d<domain>",
134 io_form_gfdda = 2,
135 gfdda_end_h = 1104, 24, 24,
136 gfdda_interval_m = 360, 360, 360,
137 fgdt = 0, 0, 0,
138 fgdtzero = 0, 0, 0,
139 if_no_pbl_nudging_uv = 0, 0, 0,
140 if_no_pbl_nudging_t = 0, 0, 0,
141 if_no_pbl_nudging_q = 0, 0, 0,
142 if_no_pbl_nudging_ph = 0, 0, 0,
143 if_zfac_uv = 0, 0, 0,
144 k_zfac_uv = 10, 10, 10,
145 if_zfac_t = 0, 0, 0,
146 k_zfac_t = 10, 10, 10,
147 if_zfac_q = 0, 0, 0,
148 k_zfac_q = 10, 10, 10,
149 if_zfac_ph = 0, 0, 0,
150 k_zfac_ph = 10, 10, 10,
151 dk_zfac_uv = 1, 1, 1,
152 dk_zfac_t = 1, 1, 1,
153 dk_zfac_q = 1, 1, 1,
154 dk_zfac_ph = 1, 1, 1,
155 guv = 0.0003, 0.0003, 0.0003,
156 gt = 0.0003, 0.0003, 0.0003,
157 gq = 0.0003, 0.0003, 0.0003,
158 gph = 0.0003, 0.0003, 0.0003,
159 !domain size [km] / wavenum ~ = 1000 km
160 xwavenum = 2,
161 ywavenum = 2,
162 if_ramping = 1,
163 dtramp_min = 60.0,
164 /
165
166 &dynamics
167 rk_ord = 3,
168 w_damping = 1,
169 diff_opt = 1, 1, 1,
170 km_opt = 4, 4, 4,
171 diff_6th_opt = 0, 0, 0,

```

APPENDIX

```

172 | diff_6th_factor      = 0.12, 0.12, 0.12,
173 | base_temp           = 290.
174 | damp_opt            = 0,
175 | zdamp               = 5000., 5000., 5000.,
176 | dampcoef            = 0.01, 0.01, 0.01,
177 | khdif               = 0, 0, 0,
178 | kvdif               = 0, 0, 0,
179 | non_hydrostatic     = .true., .true., .true.,
180 | moist_adv_opt       = 2, 2, 2,
181 | scalar_adv_opt      = 2, 2, 2,
182 | chem_adv_opt        = 2, 2, 2,
183 | tke_adv_opt         = 2, 2, 2,
184 | time_step_sound     = 4, 4, 4,
185 | h_mom_adv_order     = 5, 5, 5,
186 | v_mom_adv_order     = 3, 3, 3,
187 | h_sca_adv_order     = 5, 5, 5,
188 | v_sca_adv_order     = 3, 3, 3,
189 | /
190 |
191 | &bdy_control
192 |   spec_bdy_width    = 5,
193 |   spec_zone         = 1,
194 |   relax_zone        = 4,
195 |   specified         = .true., .false., .false.,
196 |   nested            = .false., .true., .true.,
197 | /
198 |
199 | &grib2
200 | /
201 |
202 | &namelist_quilt
203 |   nio_tasks_per_group = 0,
204 |   nio_groups = 1,
205 | /
206 |
207 | &chem
208 |   kemit              = 1,
209 |   chem_opt           = 202, 202,
210 |   bioemdt            = 30, 30, 30,
211 |   photdt             = 30, 30, 30,
212 |   chemdt             = 6, 6, 6,
213 |   io_style_emissions = 2,
214 |   emiss_inpt_opt     = 102, 102, 102,
215 |   emiss_opt          = 10, 10, 10,
216 |   emiss_opt_vol      = 0,
217 |   emiss_ash_hgt      = 20000.,
218 |   chem_in_opt        = 1, 1, 1,
219 |   phot_opt           = 1, 1, 1,
220 |   is_full_tuv        = .false.,
221 |   gas_drydep_opt     = 1, 1, 1,
222 |   aer_drydep_opt     = 1, 1, 1,
223 |   bio_emiss_opt      = 3, 3, 3,
224 |   ne_area            = 360,
225 |   dust_opt           = 3,
226 |   dmsemis_opt        = 1,
227 |   seas_opt           = 2,
228 |   depo_fact          = 0.25, 0.25, 0.25,
229 |   gas_bc_opt         = 0, 16, 16,
230 |   gas_ic_opt         = 0, 16, 16,

```

```
231 aer_bc_opt           = 1, 1, 1,
232 aer_ic_opt           = 1, 1, 1,
233 gaschem_onoff        = 1, 1, 1,
234 aerchem_onoff        = 1, 1, 1,
235 wetscav_onoff        = 1, 1, 1,
236 cldchem_onoff        = 1, 1, 1,
237 vertmix_onoff        = 1, 1, 1,
238 chem_conv_tr         = 1, 1, 1,
239 conv_tr_wetscav      = 1, 1, 1,
240 conv_tr_aqchem       = 1, 1, 1,
241 biomass_burn_opt     = 3, 3, 3,
242 plumerisefire_frq    = 30, 30, 30,
243 have_bcs_chem        = .true., true., true.,
244 have_bcs_upper       = .false., false., false.,
245 aer_ra_feedback      = 1, 1, 1,
246 aer_op_opt           = 0,
247 opt_pars_out         = 1,
248 diagnostic_chem      = 0, 0, 0,
249 /
```

Listing 2: hermes.conf

```
1 [GENERAL]
2 log_level = 3
3 input_dir = path_to_hermesv3_gr
4 data_path = path_to_hermesv3_gr/cams_glob_ant/2022
5 output_dir = path_to_hermes3_gr/hermes_out/final
6 output_name = HERMESv3_d01.<date>.nc
7 start_date = 2022/05/15 00:00:00
8 # ***** end_date = 2022/07/01 00:00:00
9 end_date = 2022/07/01 00:00:00
10 # ***** output_timestep_type = [hourly, daily, monthly, yearly] *****
11 output_timestep_type = hourly
12 output_timestep_num = 24
13 output_timestep_freq = 1
14 first_time = 0
15 erase_auxiliary_files = 0
16 # Compression level from 0 to 9; 0 corresponds to no compression and 9 to maximum
    compression
17 compression_level = 4
18
19 [DOMAIN]
20
21 # ***** output_model = [MONARCH, CMAQ, WRF_CHEM] *****
22 # output_model = MONARCH
23 # output_model = CMAQ
24 output_model = WRF_CHEM
25 output_attributes = <input_dir>/data/global_attributes.csv
26
27 # domain_type=[lcc, rotated, mercator, regular, rotated_nested]
28 domain_type = lcc
29 vertical_description = <input_dir>/data/profiles/vertical/
    WRF_CHEM_15layers_vertical_description.csv
30 auxiliary_files_path = <input_dir>/data/auxiliar_files/<domain_type>-<resolution>
31
32 # if domain_type == global:
33     # inc_lat = 1.
34     # inc_lon = 1.40625
35
36 # if domain_type == regular:
37     #lat_orig = 30.
38     #lon_orig = -30.
39     #inc_lat = 0.05
40     #inc_lon = 0.1
41     #n_lat = 840
42     #n_lon = 900
43
44
45 # if domain_type == rotated:
46     #centre_lat = 35.0
47     #centre_lon = 20.0
48     #west_boundary = -51
49     #south_boundary = -35
50     #inc_rlat = 0.1
51     #inc_rlon = 0.1
52
53 # if domain_type == rotated_nested:
54     #parent_grid_path = /scratch/Earth/ctena/temporal_coords.nc
55     #parent_ratio = 4
56     #i_parent_start = 266
```

```
57 #j-parent_start = 164
58 #n_rlat = 212
59 #n_rlon = 196
60
61 # if domain_type == lcc :
62     lat_1 = 30.0 # TRUELAT1
63     lat_2 = 60.0 # TRUELAT2
64     lon_0 = 8.800000190734863 # STANDLON
65     lat_0 = 53.0000114440918 # MOAD.CEN.LAT
66     nx = 60 # WEST-EAST.PATCH.END.UNSTAG
67     ny = 60 # SOUTH-NORTH.PATCH.END.UNSTAG
68     inc_x = 30000.0 # DX
69     inc_y = 30000.0 # DY
70     x_0 = -884999.4060587162 # x Distance [m] in Grid to bottom left point
71     y_0 = -885000.5239952778 # y Distance [m] in Grid to bottom left point
72
73 # if domain_type == mercator :
74     #lat_ts = -1.5
75     #lon_0 = -18.0
76     #nx = 210
77     #ny = 236
78     #inc_x = 50000
79     #inc_y = 50000
80     #x_0 = -126017.5
81     #y_0 = -5407460.0
82
83
84 [EMISSION_INVENTORY_CONFIGURATION]
85
86 cross_table = <input_dir>/conf/configuration.csv
87
88 [EMISSION_INVENTORY_PROFILES]
89
90 p_vertical = <input_dir>/data/profiles/vertical/Vertical_profile.csv
91 p_month = <input_dir>/data/profiles/temporal/TemporalProfile_Monthly.csv
92 p_week = <input_dir>/data/profiles/temporal/TemporalProfile_Weekly.csv
93 p_day = <input_dir>/data/profiles/temporal/TemporalProfile_Daily.csv
94 p_hour = <input_dir>/data/profiles/temporal/TemporalProfile_Hourly.csv
95 p_speciation = <input_dir>/data/profiles/speciation/
96     Speciation_profile_mozart_WRF_CHEM.csv
97
98 molecular_weights = <input_dir>/data/profiles/speciation/
99     MolecularWeightsMozartMosaic.csv
100 world_info = <input_dir>/data/profiles/temporal/tz_world_country_iso3166.csv
101 countries_shapefile = <input_dir>/data/gadm-country_mask/gadm_country_ISO3166.shp
```

Listing 3: flexpart.input

```

1 =====FORMER PATHNAMES FILE=====
2 path_to_output
3 path_to_wrf_input
4 path_to_available_file
5 =====
6 =====FORMER COMMAND FILE=====
7      1          LDIRECT:          1 for forward simulation, -1 for backward
      simulation
8 20220622 000000 YYYYMMDD HHMISS beginning date of simulation
9 20220622 230000 YYYYMMDD HHMISS ending date of simulation
10      600          SSSSS (int)      output every SSSSS seconds
11      600          SSSSS (int)      time average of output (in SSSSS seconds)
12      60           SSSSS (int)      sampling rate of output (in SSSSS seconds)
13      10800         SSSSS (int)      time constant for particle splitting (in
      seconds)
14      60           SSSSS (int)      synchronisation interval of flexpart (in
      seconds)
15      10.          CTL (real)       factor by which time step must be smaller
      than tl
16      30           IFINE (int)      decrease of time step for vertical motion by
      factor ifine
17      1           IOUT              1 concentration, 2 mixing ratio, 3 both, 4
      plume traject, 5=1+4
18      0           IPOUT            particle dump: 0 no, 1 every output interval
      , 2 only at end
19      1           LSUBGRID         subgrid terrain effect parameterization: 1
      yes, 0 no
20      0           LCONVECTION      convection: 3 yes, 0 no
21      600.         DT.CONV (real)   time interval to call convection, seconds
22      0           LAGESPECTRA     age spectra: 1 yes, 0 no
23      0           IPIN             continue simulation with dumped particle
      data: 1 yes, 0 no
24      0           IFLUX            calculate fluxes: 1 yes, 0 no
25      0           IOUTPUTFOREACHREL CREATE AN OUPUT FILE FOR EACH RELEASE
      LOCATION: 1 YES, 0 NO
26      0           MDOMAINFILL     domain-filling trajectory option: 1 yes, 0
      no, 2 strat. o3 tracer
27      1           IND.SOURCE       1=mass unit, 2=mass mixing ratio unit
28      2           IND.RECEPTOR   1=mass unit, 2=mass mixing ratio unit
29      0           NESTED.OUTPUT    shall nested output be used? 1 yes, 0 no
30      0           LINIT.COND      INITIAL COND. FOR BW RUNS: 0=NO,1=MASS UNIT
      ,2=MASS MIXING RATIO UNIT
31      1           TURB.OPTION      0=no turbulence; 1=diagnosed as in
      flexpart_ecmwf; 2 and 3=from tke.
32      1           LU.OPTION        0=old landuse (IGBP.dat); 1=landuse from WRF
33      1           CBL SCHEME       0=no, 1=yes. works if TURB.OPTION=1
34      0           SFC.OPTION       0=default computation of u*, hflux, pblh, 1=
      from wrf
35      0           WIND.OPTION      0=snapshot winds, 1=mean winds,2=snapshot
      eta-dot,-1=w based on divergence
36      0           TIME.OPTION      1=correction of time validity for time-
      average wind, 0=no need
37      1           OUTGRID.COORD    0=wrf grid(meters), 1=regular lat/lon grid
38      1           RELEASE.COORD    0=wrf grid(meters), 1=regular lat/lon grid
39      2           IOUTTYPE         0=default binary, 1=ascii (for particle dump
      only),2=netcdf
40      999          NCTIMEREC (int) Time frames per output file, only used for
      netcdf

```

```

41      100                VERBOSE                VERBOSE MODE,0=minimum, 100=maximum
42  =====FORMER AGECLASSESS FILE=====
43      1                NAGECLASS                number of age classes
44      999999           SSSSSS (int)            age class in SSSSS seconds
45  =====FORMER OUTGRID FILE=====
46  8.1                OUTLONLEFT                geographical longitude of lower left corner of output
         grid ###half grid box in m
47  52.8              OUTLATLOWER                geographical latitude of lower left corner of output
         grid ##half gridbox in m
48  90                NUMXGRID                number of grid points in x direction (= # of cells )
49  90                NUMYGRID                number of grid points in y direction (= # of cells )
50  1                OUTGRIDDEF                outgrid defined 0=using grid distance, 1=upperright
         corner coordinate
51  9.6                DXOUTLON                grid distance(in DEG!) in x direction or upper right
         corner of output grid ### gridboxes*gridres in m + half grid box
52  53.7              DYOUTLAT                grid distance(in DEG!) in y direction or upper right
         corner of output grid
53  32                NUMZGRID                number of vertical levels
54  69.8              LEVEL                    height of level (upper boundary)
55  135.3             LEVEL                    height of level (upper boundary)
56  218.8             LEVEL                    height of level (upper boundary)
57  324.8             LEVEL                    height of level (upper boundary)
58  458.1             LEVEL                    height of level (upper boundary)
59  623.9             LEVEL                    height of level (upper boundary)
60  827.5             LEVEL                    height of level (upper boundary)
61  1074.2            LEVEL                    height of level (upper boundary)
62  1368.3            LEVEL                    height of level (upper boundary)
63  1712.9            LEVEL                    height of level (upper boundary)
64  2109.0            LEVEL                    height of level (upper boundary)
65  2555.9            LEVEL                    height of level (upper boundary)
66  3050.9            LEVEL                    height of level (upper boundary)
67  3592.1            LEVEL                    height of level (upper boundary)
68  4180.3            LEVEL                    height of level (upper boundary)
69  4817.6            LEVEL                    height of level (upper boundary)
70  5506.7            LEVEL                    height of level (upper boundary)
71  6249.8            LEVEL                    height of level (upper boundary)
72  7048.5            LEVEL                    height of level (upper boundary)
73  7903.6            LEVEL                    height of level (upper boundary)
74  8813.8            LEVEL                    height of level (upper boundary)
75  9778.2            LEVEL                    height of level (upper boundary)
76  10802.6           LEVEL                    height of level (upper boundary)
77  11878.6           LEVEL                    height of level (upper boundary)
78  12972.6           LEVEL                    height of level (upper boundary)
79  14064.8           LEVEL                    height of level (upper boundary)
80  15159.1           LEVEL                    height of level (upper boundary)
81  16259.9           LEVEL                    height of level (upper boundary)
82  17367.9           LEVEL                    height of level (upper boundary)
83  18481.0           LEVEL                    height of level (upper boundary)
84  19595.6           LEVEL                    height of level (upper boundary)
85  20710.0           LEVEL                    height of level (upper boundary)
86  =====FORMER RECEPTOR FILE=====
87  0                NUMRECEPTOR            number of receptors
88  =====FORMER SPECIES FILE=====
89  1                NUMTABLE                number of variable properties. The following lines
         are fixed format
90  XXXX|NAME        |decaytime | wetscava | wetsb| drydif| dryhenry| drya| partrho | parmean|
         partsig| dryvelo| weight | ohreact |
91      NOx          14940          -9.9   -9.9   -9.9          -9.9E-9
         -9.99  46.000          -9.9E-09

```

APPENDIX

	FORMER RELEASES FILE		
92			
93	1	NSPEC	total number of species emitted
94	0	EMITVAR	1 for emission variation
95	1	LINK	index of species in file SPECIES
96	1	NUMPOINT	number of releases
97	20220622 000000	ID1, IT1	beginning date and time of release
98	20220622 230000	ID2, IT2	ending date and time of release
99	8.818107	XPOINT1 (real)	longitude [deg] of lower left corner
100	53.114664	YPOINT1 (real)	latitude [deg] of lower left corner
101	8.818107	XPOINT2 (real)	longitude [deg] of upper right corner
102	53.114664	YPOINT2 (real)	latitude [DEG] of upper right corner
103	1	KINDZ (int)	1 for m above ground, 2 for m above sea level, 3 pressure
104	75.000	ZPOINT1 (real)	lower z-level
105	75.000	ZPOINT2 (real)	upper z-level
106	1000000	NPART (int)	total number of particles to be released
107	1071.23	XMASS (real)	total mass emitted
108	swb.incineration_plant		NAME OF RELEASE LOCATION

Offizielle Erklärungen von

Name: _____ Matrikelnr.: _____

Eigenständigkeitserklärung

Ich versichere, dass ich die vorliegende Arbeit selbstständig verfasst und keine anderen als die angegebenen Quellen und Hilfsmittel verwendet habe.

Alle Teile meiner Arbeit, die wortwörtlich oder dem Sinn nach anderen Werken entnommen sind, wurden unter Angabe der Quelle kenntlich gemacht. Gleiches gilt auch für Zeichnungen, Skizzen, bildliche Darstellungen sowie für Quellen aus dem Internet.

Die Arbeit wurde in gleicher oder ähnlicher Form noch nicht als Prüfungsleistung eingereicht.

Die elektronische Fassung der Arbeit stimmt mit der gedruckten Version überein.

Mir ist bewusst, dass wahrheitswidrige Angaben als Täuschung behandelt werden.

A) Erklärung zur Veröffentlichung von Bachelor- oder Masterarbeiten

Die Abschlussarbeit wird zwei Jahre nach Studienabschluss dem Archiv der Universität Bremen zur dauerhaften Archivierung angeboten. Archiviert werden:

- 1) Masterarbeiten mit lokalem oder regionalem Bezug sowie pro Studienfach und Studienjahr 10 % aller Abschlussarbeiten
- 2) Bachelorarbeiten des jeweils ersten und letzten Bachelorabschlusses pro Studienfach u. Jahr.

- Ich bin damit einverstanden, dass meine Abschlussarbeit im Universitätsarchiv für wissenschaftliche Zwecke von Dritten eingesehen werden darf.
- Ich bin damit einverstanden, dass meine Abschlussarbeit nach 30 Jahren (gem. §7 Abs. 2 BremArchivG) im Universitätsarchiv für wissenschaftliche Zwecke von Dritten eingesehen werden darf.
- Ich bin nicht damit einverstanden, dass meine Abschlussarbeit im Universitätsarchiv für wissenschaftliche Zwecke von Dritten eingesehen werden darf.

B) Einverständniserklärung über die Bereitstellung und Nutzung der Bachelorarbeit / Masterarbeit / Hausarbeit in elektronischer Form zur Überprüfung durch Plagiatsoftware

Eingereichte Arbeiten können mit der Software *Plagscan* auf einem hauseigenen Server auf Übereinstimmung mit externen Quellen und der institutionseigenen Datenbank untersucht werden.

Zum Zweck des Abgleichs mit zukünftig zu überprüfenden Studien- und Prüfungsarbeiten kann die Arbeit dauerhaft in der institutionseigenen Datenbank der Universität Bremen gespeichert werden.

- Ich bin damit einverstanden, dass die von mir vorgelegte und verfasste Arbeit zum Zweck der Überprüfung auf Plagiate auf den *Plagscan*-Server der Universität Bremen hochgeladen wird.
- Ich bin ebenfalls damit einverstanden, dass die von mir vorgelegte und verfasste Arbeit zum o.g. Zweck auf dem *Plagscan*-Server der Universität Bremen hochgeladen u. dauerhaft auf dem *Plagscan*-Server gespeichert wird.
- Ich bin nicht damit einverstanden, dass die von mir vorgelegte u. verfasste Arbeit zum o.g. Zweck auf dem *Plagscan*-Server der Universität Bremen hochgeladen u. dauerhaft gespeichert wird.

Mit meiner Unterschrift versichere ich, dass ich die obenstehenden Erklärungen gelesen und verstanden habe. Mit meiner Unterschrift bestätige ich die Richtigkeit der oben gemachten Angaben.

Datum, Ort

Unterschrift